



**HAL**  
open science

# Structure of North American mantle constrained by simultaneous inversion of multiple-frequency SH, SS, and Love waves

Y. Tian, Y. Zhou, K. Sigloch, G. Nolet, G. Laske

► **To cite this version:**

Y. Tian, Y. Zhou, K. Sigloch, G. Nolet, G. Laske. Structure of North American mantle constrained by simultaneous inversion of multiple-frequency SH, SS, and Love waves. *Journal of Geophysical Research*, 2011, 116, pp.B02307. 10.1029/2010JB007704 . hal-00585759

**HAL Id: hal-00585759**

**<https://hal.science/hal-00585759>**

Submitted on 2 Oct 2021

**HAL** is a multi-disciplinary open access archive for the deposit and dissemination of scientific research documents, whether they are published or not. The documents may come from teaching and research institutions in France or abroad, or from public or private research centers.

L'archive ouverte pluridisciplinaire **HAL**, est destinée au dépôt et à la diffusion de documents scientifiques de niveau recherche, publiés ou non, émanant des établissements d'enseignement et de recherche français ou étrangers, des laboratoires publics ou privés.

Copyright

# Structure of North American mantle constrained by simultaneous inversion of multiple-frequency *SH*, *SS*, and Love waves

Yue Tian,<sup>1,2</sup> Ying Zhou,<sup>3</sup> Karin Sigloch,<sup>4</sup> Guust Nolet,<sup>5</sup> and Gabi Laske<sup>6</sup>

Received 16 May 2010; revised 12 November 2010; accepted 3 December 2010; published 15 February 2011.

[1] We simultaneously invert for the velocity and attenuation structure of the North American mantle from a mixed data set: *SH* wave traveltimes and amplitude anomalies, *SS* wave differential traveltimes anomalies, and Love wave fundamental mode phase delays. All data are measured for multiple frequency bands, and finite frequency sensitivity kernels are used to explain the observations. In the resulting *SH* velocity model, a lower mantle plume is observed to originate at about 1500 km depth beneath the Yellowstone area, tilting about 40° from vertical. The plume rises up through a gap in the subducting Farallon slab. The *SH* velocity model confirms high-level segmentation of the Farallon slab, which was observed in the recent *P* velocity model. Attenuation structure is resolvable in the upper mantle and transition zone; in estimating it, we correct for focusing. High-correlation coefficients between  $\delta \ln V_S$  and  $\delta \ln Q_S$  under the central and eastern United States suggest one main physical source, most likely temperature. The smaller correlation coefficients and larger slopes of the  $\delta \ln Q_S - \delta \ln V_S$  relationship under the western United States suggest an influence of nonthermal factors such as the existence of water and partial melt. Finally, we analyze the influence of the different components of our data set. The addition of Love wave phase delays helps to improve the resolution of both velocity and attenuation, and the effect is noticeable even in the lower mantle.

**Citation:** Tian, Y., Y. Zhou, K. Sigloch, G. Nolet, and G. Laske (2011), Structure of North American mantle constrained by simultaneous inversion of multiple-frequency *SH*, *SS*, and Love waves, *J. Geophys. Res.*, 116, B02307, doi:10.1029/2010JB007704.

## 1. Introduction

[2] Recent progress in high-resolution tomography has led to a clearer view of subduction history and slab geometry: subducted slabs may be torn apart and segmented [Nolet, 2009]. The Farallon slab shows evidence of segmentation under North America. Various hypotheses for the deformation of the Farallon slab have been proposed, including “slab buckling” [Humphreys, 1995] and “slab roll back” followed by detachment [van der Lee and Nolet, 1997a]. Sigloch *et al.* [2008] present the clearest evidence so far for high-level segmentation of the Farallon slab, an

observation that was supported by *P* and *S* wave studies by Roth *et al.* [2008], Burdick *et al.* [2009], Tian *et al.* [2009], Xue and Allen [2010], and Obrebski *et al.* [2010]. The way in which the Farallon slab broke up into fragments has direct effects on subduction dynamics, by controlling the width of the slab and thus the trench migration rates [Schellart *et al.*, 2007] which in turn influences the ability of the slab to enter the lower mantle [Goes *et al.*, 2008]. The observed tears in the Farallon slab allow for mantle upwellings and thus may contribute to explain the widespread and complex patterns of magmatism in the western United States [Smith and Luedke, 1984]. Tomographic studies of the mantle beneath North America are necessary to examine how the Farallon slab deformed and fragmented. Our study serves this purpose.

[3] Comparisons between attenuation and velocity heterogeneities provide further insight into the physical state of the mantle, because different physical sources for mantle heterogeneity, such as temperature [e.g., Karato, 1993; Jackson *et al.*, 2002], water content [e.g., Karato, 2006], partial melt [e.g., Jackson *et al.*, 2004; Faul *et al.*, 2004], chemical composition [e.g., Lee, 2003], and grain size [e.g., Faul and Jackson, 2005], give different attenuation-velocity relationships. There have been few tomographic studies on the attenuation structure of North American mantle.

<sup>1</sup>Department of Geosciences, Princeton University, Princeton, New Jersey, USA.

<sup>2</sup>Now at Chevron Energy Technology Company, San Ramon, California, USA.

<sup>3</sup>Department of Geosciences, Virginia Polytechnic Institute and State University, Blacksburg, Virginia, USA.

<sup>4</sup>Department of Earth and Environmental Sciences, Munich University, Munich, Germany.

<sup>5</sup>Géosciences Azur, Université de Nice/Antipolis, Sophia Antipolis, France.

<sup>6</sup>Institute of Geophysics and Planetary Physics, University of California, San Diego, La Jolla, California, USA.

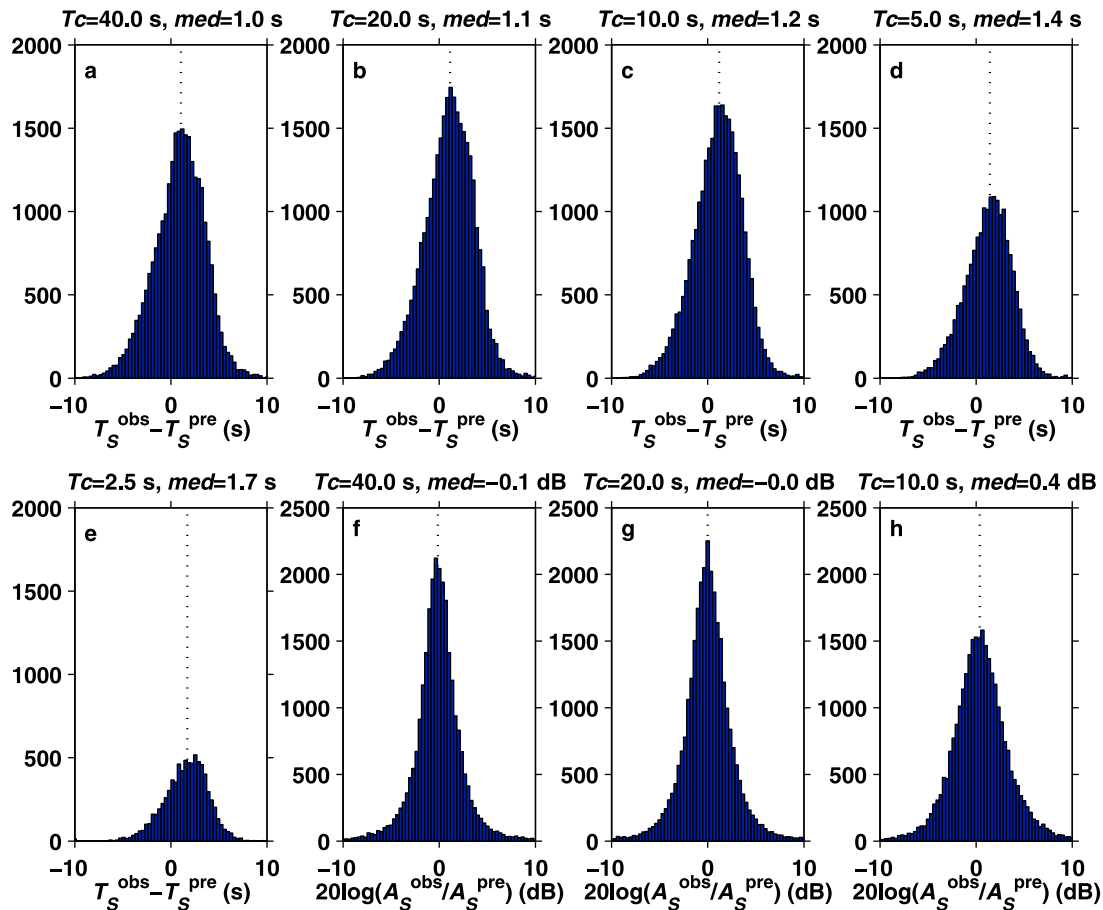


**Figure 1.** Histograms of  $SH$  wave measurements used in this study (before applying ellipticity, elevation, and crustal corrections). (a–e) Traveltime anomalies defined as the difference between the observed arrival time  $T_S^{\text{obs}}$  and the predicted arrival time  $T_S^{\text{pre}}$ . (f–h) Amplitude anomalies defined as the ratio between the observed amplitude  $A_S^{\text{obs}}$  and the predicted amplitude  $A_S^{\text{pre}}$ , in decibels. The heading indicates the center period of the frequency band ( $T_c$ ) and the median of the measurements in that band ( $med$ ).

Lawrence *et al.* [2006] mapped the two-dimensional  $P$  and  $S$   $t^*$  residuals under North America but with no depth constraints. Yang and Forsyth [2008] simultaneously inverted for one-dimensional  $V_S$  and  $Q_\mu$  structure of the upper mantle beneath southern California. Hwang *et al.* [2009] estimated the two-dimensional  $P$  wave  $t^*$  structure under North America with no depth constraints. The first joint inversion for three-dimensional  $V_P$  and  $Q_P$  structure under North America was conducted by Sigloch *et al.* [2008]. The first joint inversion for three-dimensional  $V_S$  and  $Q_S$  structure under the western United States was carried out by Tian *et al.* [2009], using multiple-frequency  $SH$  wave traveltimes and amplitudes.

[4] The current study extends the work by Tian *et al.* [2009] by including  $SS$  wave delays and Love wave phase data and imaging the mantle under North America. We simultaneously estimate the  $SH$  wave velocity and attenuation structure under North America, taking advantage of three recent developments in seismology: (1) the large volume of data provided by the USArray which has densely sampled the western United States; (2) finite frequency sensitivity theory and the fast computation of the sensitivity kernels for body wave traveltimes [Dahlen *et al.*, 2000], focusing effects [Dahlen and Baig, 2002], attenuation

[Nolet, 2008, section 8.5], and surface waves [Zhou *et al.*, 2004]; and (3) accurate techniques to measure frequency-dependent body wave traveltimes and amplitudes [Sigloch and Nolet, 2006] and surface wave phase delays [Laske and Masters, 1996]. The velocity model is used to study the mantle dynamics under North America. The velocity and attenuation models are compared to gain insight into the sources of mantle heterogeneities. Effects of adding new types of data, especially the Love wave phase delays, are also investigated.

## 2. The Data Set

[5] We use a mixed data set consisting of four different types of data, which are all measured at multiple frequencies from the transverse component:  $SH$  wave traveltime anomalies,  $SH$  wave amplitude anomalies,  $SS$  wave differential traveltime anomalies, and Love wave fundamental mode phase delays. This data set is an extension of the  $SH$  data set built by Tian *et al.* [2009], to which we add (1) Love wave phase delays, (2)  $SS$  wave differential delays, and (3) more  $SH$  wave measurements from most recent USArray stations. Love waves are particularly helpful. They provide the depth resolution which body waves lack because

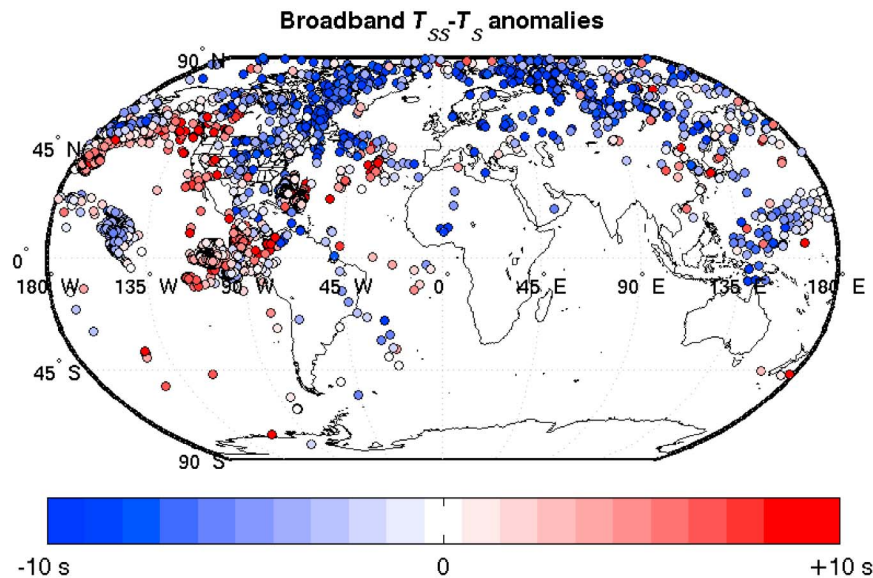


**Figure 2.** Broadband  $SS$  wave differential traveltime anomalies  $\delta(T_{SS} - T_S)$  plotted at each reflection point. Positive values reflect slow velocity anomalies in the vicinity of the reflection point, and negative values indicate fast velocity anomalies.

in the shallow region the teleseismic body wave paths are almost vertical.  $SS$  waves help to improve the resolution with reflection points covering regions not sampled by direct  $SH$  waves.

### 2.1. $SH$ Wave Traveltime and Amplitude Anomalies

[6] We construct a global data set of  $SH$  wave traveltime anomalies

$$\delta T_S = T_S^{\text{obs}} - T_S^{\text{pre}} \quad (1)$$

and amplitude anomalies

$$\delta \ln A_S = A_S^{\text{obs}} / A_S^{\text{pre}} - 1 \quad (2)$$

(with “obs” for observed and “pre” for predicted data) in five frequency bands with center periods of 40, 20, 10, 5, and 2.5 s, respectively (see *Tian et al.* [2009] for the pass-band filter responses). The measurements are obtained through cross correlation, using the technique developed by *Sigloch and Nolet* [2006]. These measurements are deviations from predictions computed for the IASP91  $V_S$  model [*Kennett and Engdahl*, 1991] extended with the PREM  $Q_S$  model [*Dziewonski and Anderson*, 1981]. Details of how to construct the data set and discussions of the frequency dependence and spatial distribution of the data set are described by *Tian et al.* [2009]. In this paper, we update the  $SH$  wave data set with more recent USArray data until October 2008. The current  $SH$  data set consists of 26,296 wave paths, producing 98,371 acceptable traveltime measurements in the five frequency bands and 74,665 acceptable amplitude measurements in the three low-frequency bands. For an idea of the  $SH$  data coverage in North America, see Figures 5c–5e and 6c–6e.

[7] The use of cross correlation for the estimation of delays allows us to exploit the different sensitivity of high and low frequencies. A small heterogeneity may not show up in

a low-frequency delay because of the effects of wavefront healing [*Nolet and Dahlen*, 2000], but it may still be visible at high frequency. Delay dispersion thus provides information on the size of velocity heterogeneity. The histograms of delays in Figure 1 show a frequency dependence of the data: the median of traveltime anomalies and the median and standard deviation of amplitude anomalies increase with frequency. To interpret the frequency dependence of delays and amplitude anomalies, we use finite frequency sensitivity kernels.

### 2.2. $SS$ Wave Differential Traveltime Anomalies

[8] We measure the  $SS$  wave differential traveltime anomalies

$$\delta(T_{SS} - T_S) = (T_{SS} - T_S)^{\text{obs}} - (T_{SS} - T_S)^{\text{pre}} \quad (3)$$

in the same five frequency bands as for  $SH$  waves. The observed differential traveltimes  $(T_{SS} - T_S)^{\text{obs}}$  are measured by cross-correlating the observed  $SS$  waveform with the predicted  $SS$  waveform. The predicted  $SS$  waveform is computed by Hilbert transforming the observed  $SH$  waveform, applying the attenuation operator to account for the difference in attenuation along the  $SS$  and  $SH$  paths, and multiplication by  $-1$  to account for the reflection at the free surface. Both the observed and predicted  $SS$  waveforms are filtered in each of the five frequency bands, and the cross correlation is done in each band.

[9] We measure any  $SS$  wave that has a corresponding acceptable measurement of  $\delta T_S$  (see section 2.1) and that has an epicentral distance between  $60^\circ$  and  $88^\circ$ . The quality of acceptable  $\delta T_S$  guarantees reliable estimates of the  $SH$  wave window and source depth, which are used to compute the predicted  $SS$  waveform. The lower limit of  $60^\circ$  is to exclude triplications of  $SS$ , and the upper limit of  $88^\circ$  is to exclude  $D''$  and CMB diffracted  $SH$  waves [*Paulssen and Stutzmann*, 1996]. Measurements are deemed acceptable by visual

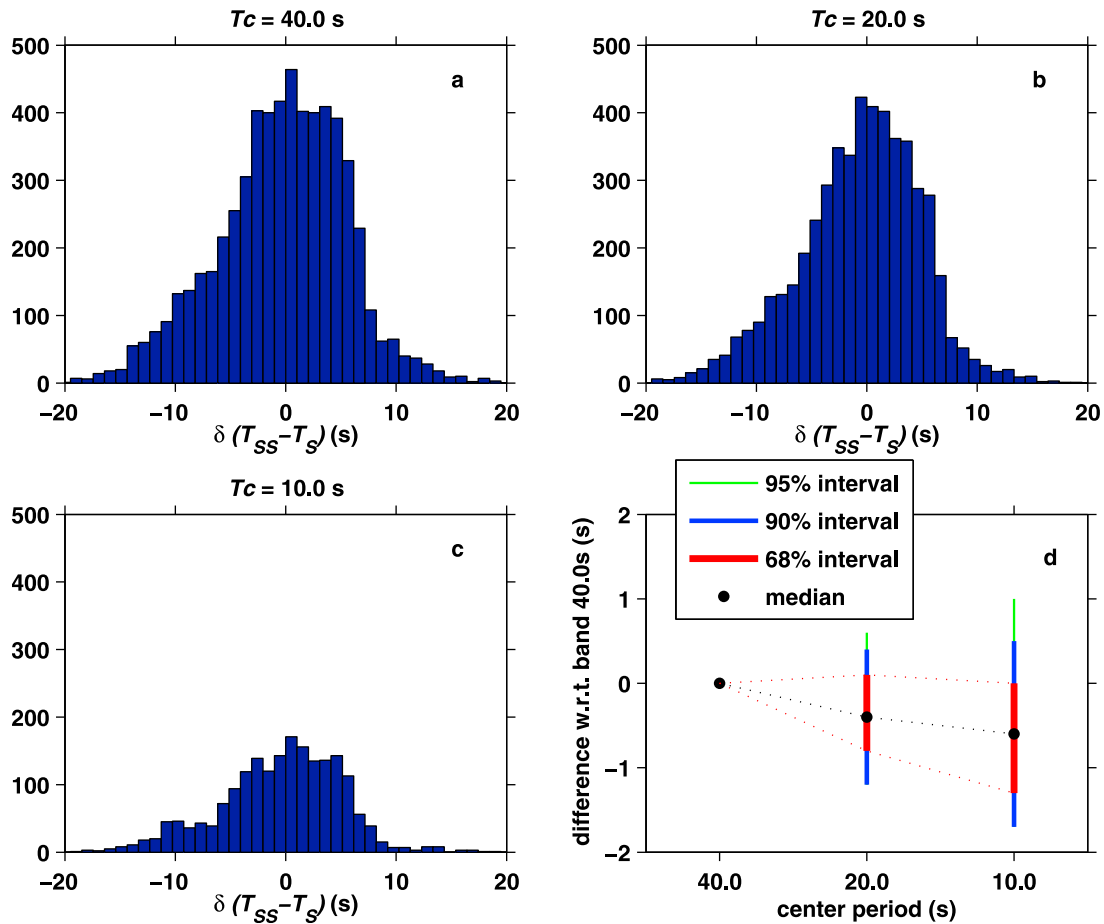


**Figure 3.** (a–c) Histograms of  $SS$  wave differential traveltime anomalies  $\delta(T_{SS} - T_S)$  used in this study (after applying ellipticity, elevation, and crustal corrections).  $T_c$  indicates the center period of the frequency band. (d) Dispersion of  $\delta(T_{SS} - T_S)$ . On the horizontal axis, each frequency band is represented by its center period. The vertical axis is the difference between  $\delta(T_{SS} - T_S)$  in one band and  $\delta(T_{SS} - T_S)$  in band 40 s. Only wave paths that have acceptable measurements in all three bands are used to produce the plot. The black dot, red bar, blue bar, and green bar represent the median, 68% interval, 90% interval, and 95% interval of the dispersion, respectively.

inspection of the waveform fits after cross correlation. We impose a lower limit of 0.9 on the cross-correlation coefficient. The two high-frequency bands (with center periods of 5 s and 2.5 s) are not used for tomography because the  $(T_{SS} - T_S)^{\text{obs}}$  uncertainty estimated from pairs of closely located events is much larger in these two bands ( $\sim 1.8$  s) than in the other frequency bands ( $\sim 0.8$  s). The final  $SS$  wave data set consists of 18,919 measurements from 8270 wave paths in three frequency bands (with center periods of 40 s, 20 s, and 10 s). The  $SS$  data coverage in North America is shown in Figures 5b and 6b.

[10] To examine the consistency of the measurements, Figure 2 plots  $\delta(T_{SS} - T_S)$  at each reflection point for unfiltered (“broadband”) data, which reflects anomalies in the shallow subsurface beneath the reflection point. The map shows distinct large-scale patterns, and they correlate with tectonic structure. For example, negative anomalies at the Canadian shield and the Siberian shield, positive anomalies in western North America and western Central America. The patterns are similar to those observed by *Woodward and Masters* [1991] and *Reid et al.* [2001].

[11] After applying crustal, ellipticity, and elevation corrections, the histogram of  $SS$  differential delays in each frequency band is plotted in Figures 3a–3c. The histograms are skewed toward negative anomalies. One possible cause of this asymmetry is that more reflection points hit the region with fast shallow structure (see Figure 2). Figure 3d examines the dispersion of  $SS$  differential delays with respect to the lowest-frequency band. The dispersion is of the order of 1 s, which is of the same order as the uncertainty in  $SS$  differential delays. If the dispersion is completely due to random noise, one expects to observe a zero median and the same standard deviation in the 20 and 10 s bands. The nonzero medians in both bands and the clear trend of larger dispersion with increasing frequency difference suggest that the observed dispersion is at least partially due to the finite frequency effect, though at low-frequency crustal effects may play a role [*Ritsema et al.*, 2009].

### 2.3. Love Wave Fundamental Mode Phase Delays

[12] For Love waves, we use the fundamental mode minor arc phase delays, measured at 11 frequencies (5, 6, 7,

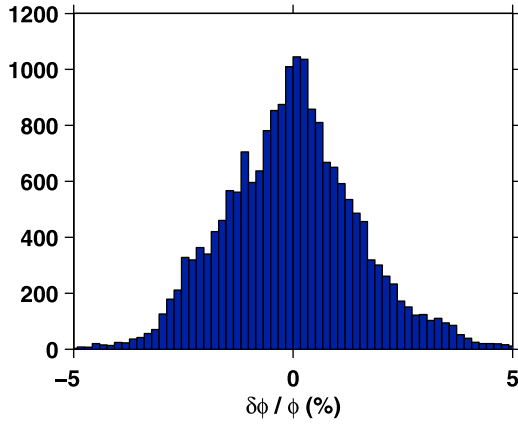


**Figure 4.** Histogram of Love wave relative phase delays  $\delta\phi/\phi$  at 11 frequencies (5, 6, 7,  $\dots$ , 15 mHz) used in this study, after applying crustal corrections.

$\dots$ , 15 mHz) with a multitaper technique [Laske and Masters, 1996]. This data set consists of 19,485 phase delays from 1778 wave paths. It is part of the global surface wave data set used by Zhou *et al.* [2006]. Figures 5a and 6a show the Love wave data coverage in North America. The original phase delays used by Zhou *et al.* [2006] are for the reference model 1066A [Gilbert and Dziewonski, 1975]. To be consistent with the body waves, the phase delays are corrected to be for the reference model IASP91 [Kennett and Engdahl, 1991]. After crustal corrections, the histograms of the relative phase delays  $\delta\ln\phi = \delta\phi/\phi$  are plotted in Figure 4.

#### 2.4. Data Corrections and Uncertainties

[13] For body waves, when computing *SH* and *SS* traveltimes, the effects of ellipticity, crustal structure, and station elevations are taken into account [Tian *et al.*, 2007a]. The crustal corrections are computed using ray theory and the three-dimensional crust model CRUST2.0 [Bassin *et al.*, 2000]. According to Ritsema *et al.* [2009] and Obayashi *et al.* [2004], the crustal correction difference  $\Delta(\delta t_C)$  between ray theoretical and finite frequency calculations are not negligible for long-period waves. This is a potential source of uncertainties for *SH* and *SS* traveltimes. Specifically, for *SH* waves, Ritsema *et al.* [2009] show that the ratio between  $\Delta(\delta t_C)$  and the RMS of measured traveltime anomalies is 0.144, 0.146, and 0.184 for 40, 20, and 10 s periods, respectively. For *SS* waves, the ratio is 0.069, 0.110, and 0.055 for 40, 20, and 10 s period, respectively. The uncertainties in  $\delta T_S$ ,  $\delta\ln A_S$ , and  $\delta(T_{SS} - T_S)$  are estimated based on (1) difference between two measurements from two closely located events at the same station; (2) variation of one measurement with cross-correlation window length; and (3) quality of the waveform fit. As a result, the  $\delta T_S$  uncertainties range from 0.6 s to 1.2 s, the  $\delta\ln A_S$  uncertainties range from 0.12 to 0.22 (0.98 to 1.73 dB or  $-2.16$  to  $-1.11$  dB), and the  $\delta(T_{SS} - T_S)$  uncertainties range from 1.1 to 1.7 s.

[14] For Love waves, the crustal structure has a very large effect on phase delays [e.g., Zhou *et al.* 2006]. Crustal corrections are computed using ray theory and the model CRUST2.0 [Bassin *et al.*, 2000], and are applied to the

phase delay measurements before inversion. We adopt the phase delay uncertainties estimated by Zhou *et al.* [2006] based on pairs of closely located events, and slightly adjust them in order to control the relative importance of different data types in the joint inversion. The uncertainty for the relative phase delay  $\delta\phi/\phi$  ranges from 0.74% to 0.93%. Regional crustal models in the western United States have been developed based upon receiver function analysis and *Pn* tomography of USArray data, and discrepancies exist among models developed by different research groups [e.g., Wilson *et al.*, 2010; Buehler and Shearer, 2010]. However, details in regional crustal structure do not have significant effects on Love wave phase delays at the periods we are interested in. For example, a 5 km difference in crustal thickness over a propagation distance of  $40^\circ$  would introduce a  $\delta\phi/\phi$  difference of less than 0.22% at 5 mHz frequency and a  $\delta\phi/\phi$  difference of less than 0.59% at 15 mHz frequency. Both are smaller than the estimated uncertainty of  $\delta\phi/\phi$ .

### 3. The Joint Finite Frequency Tomographic System

#### 3.1. The Continuous Linear System

[15] In finite frequency tomography, the linear inverse problem takes four forms corresponding to our four data types:

[16] 1. For *SH* wave traveltime anomalies, the linear inverse problem is

$$\delta T_S(s(\omega)) = \iiint K_V^{TS}(s(\omega), \mathbf{R}) \delta\ln V_S(\mathbf{R}) d^3\mathbf{R} + \delta T_0 + \delta\mathbf{X}_0 \cdot \left. \frac{\hat{\mathbf{p}}}{V_S} \right|_{\mathbf{X}_0}, \quad (4)$$

with  $\delta\ln V_S$  representing velocity heterogeneities, and the sensitivity kernel  $K_V^{TS}$  describing how the velocity heterogeneity affects *SH* wave traveltimes [Dahlen *et al.*, 2000]. Here  $s(\omega)$  is the frequency content of the observed waveform that is used to measure  $\delta T_S$ . For our data set, we assume that this is equal to the frequency response of the passband filter. The last two terms are correction terms:  $\delta T_0$  represents the origin time correction, vector  $\delta\mathbf{X}_0$  represents the hypocenter correction, and  $(\hat{\mathbf{p}}/V_S)|_{\mathbf{X}_0}$  represents the slowness vector at hypocenter  $\mathbf{X}_0$ .

[17] 2. For *SH* wave amplitude anomalies, the linear inverse problem is

$$\delta\ln A_S(s(\omega)) = \iiint K_V^{AS}(s(\omega), \mathbf{R}) \delta\ln V_S(\mathbf{R}) d^3\mathbf{R} + \iiint K_Q^{AS}(s(\omega), \mathbf{R}) \delta\ln Q_S^{-1}(\mathbf{R}) d^3\mathbf{R} + \delta\ln A_0 + \delta\ln A_r. \quad (5)$$

Here  $\delta\ln Q_S^{-1}$  represents attenuation heterogeneities. The sensitivity kernel  $K_V^{AS}$  describes how the velocity heterogeneity affects *SH* wave amplitudes [Dahlen and Baig, 2002], and  $K_Q^{AS}$  describes how the attenuation heterogeneity affects *SH* wave amplitudes [Nolet, 2008, Section 8.5].  $\delta\ln A_0$  is the source correction term accounting for the scalar moment errors and the uncertainty in source time function scaling in

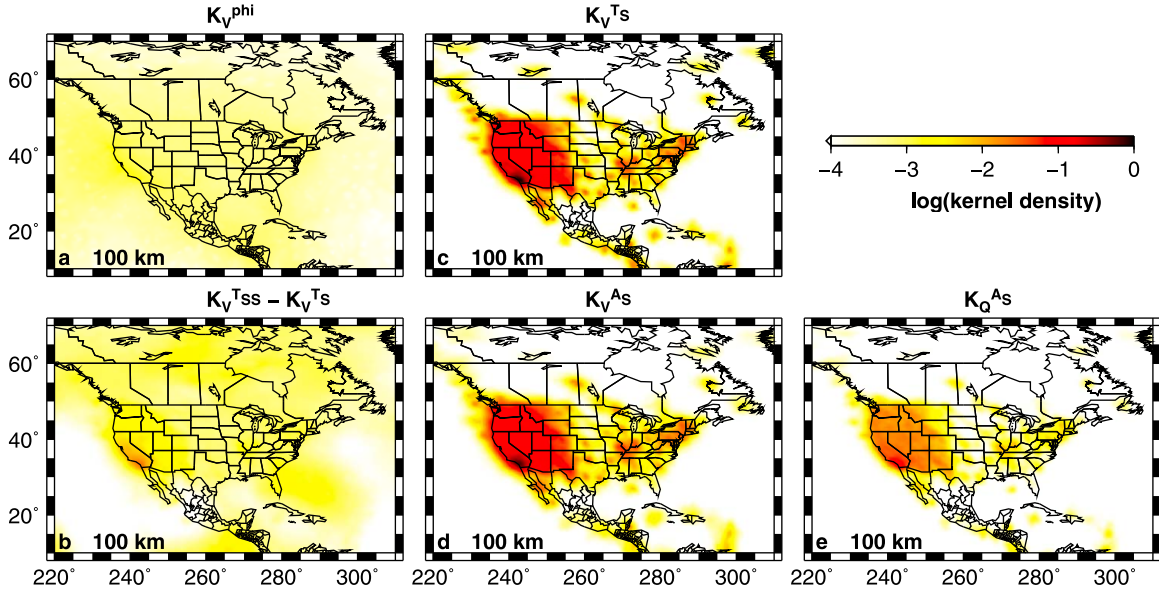


**Figure 5.** The kernel density (see equation (9)) for the five sensitivity kernels in equation (8) at 100 km depth. The heading indicates the kernel type. (a) For Love wave kernels and (b) for  $SS$  wave kernels. (c and d) For  $SH$  wave velocity kernels. (e) For  $SH$  wave attenuation kernels.

the measurement process [Sigloch and Nolet, 2006], and  $\delta \ln A_r$  is the station correction term accounting for sediment effects and adjustment of the instrument magnification.

[18] 3. For  $SS$  wave differential traveltime anomalies, the linear inverse problem is

$$\delta(T_{SS} - T_S)(s(\omega)) = \iiint (K_V^{Tss}(s(\omega), \mathbf{R}) - K_V^{Ts}(s(\omega), \mathbf{R})) \delta \ln V_S(\mathbf{R}) d^3 \mathbf{R}, \quad (6)$$

with  $K_V^{Tss}$  and  $K_V^{Ts}$  representing the  $SS$  and  $SH$  traveltime-velocity sensitivities, respectively [Dahlen et al., 2000].

[19] 4. For Love wave phase delays, the linear inverse problem is

$$\delta \ln \phi(\omega) = \iiint K_V^{\phi}(\omega, \mathbf{R}) \delta \ln V_S(\mathbf{R}) d^3 \mathbf{R} + \frac{c \delta T_0}{\Delta}. \quad (7)$$

The sensitivity kernel  $K_V^{\phi}$  describes how the velocity heterogeneity affects Love wave phase delays [Zhou et al., 2004], and  $\omega$  is the angular frequency at which  $\delta \ln \phi$  is measured. In the last term,  $\delta T_0$  is the origin time correction,  $c$  is the phase velocity in km/s, and  $\Delta$  is the epicentral distance in km.

### 3.2. The Discrete Linear System

[20] We use a model parameterization in the form of a tetrahedral mesh with linear interpolation in between grid nodes. The general philosophy of adaptive tetrahedral meshing is described by Nolet [2008, section 12.2]. Here we use the same tetrahedral mesh as in the work by Sigloch et al. [2008] and Tian et al. [2009]. Beneath the United States, the grid spacing of the mesh is about 70 km in the upper mantle, and increases to roughly 200 km at 660 km depth. Outside of the United States, the grid spacing is about 200 km in the upper mantle and transition zone. Below 660 km, the grid spacing increases linearly to about 300 km at 2000

km depth. The mesh is produced with the Matlab software distmesh developed by Persson and Strang [2004].

[21] With source and receiver correction terms and regularization, the complete discrete linear system of the tomographic problem can be written as

$$\begin{pmatrix} K_V^{Ts} & 0 & K_C^{Ts} & 0 & 0 \\ K_V^{As} & K_Q^{As} & 0 & K_C^{As} & 0 \\ K_V^{Tss} - K_V^{Ts} & 0 & 0 & 0 & 0 \\ K_V^{\phi} & 0 & 0 & 0 & K_C^{\phi} \\ \epsilon_1 W & 0 & 0 & 0 & 0 \\ 0 & \epsilon_1 W & 0 & 0 & 0 \\ 0 & 0 & \epsilon_1 W & 0 & 0 \\ 0 & 0 & 0 & \epsilon_1 W & 0 \\ 0 & 0 & 0 & 0 & \epsilon_1 W \\ \epsilon_2 RW & 0 & 0 & 0 & 0 \\ 0 & \epsilon_2 RW & 0 & 0 & 0 \end{pmatrix} \begin{pmatrix} \delta \ln V_S \\ \delta \ln Q_S^{-1} \\ C^{Ts} \\ C^{As} \\ C^{\phi} \end{pmatrix} = \begin{pmatrix} \delta T_S \\ \delta \ln A_S \\ \delta(T_{SS} - T_S) \\ \delta \ln \phi \\ 0 \\ 0 \\ 0 \\ 0 \\ 0 \\ 0 \\ 0 \end{pmatrix}. \quad (8)$$

The first four rows correspond to equations (4)–(7). The vector on the right-hand side contains in sequence the four types of data, as described in section 2. On the left-hand

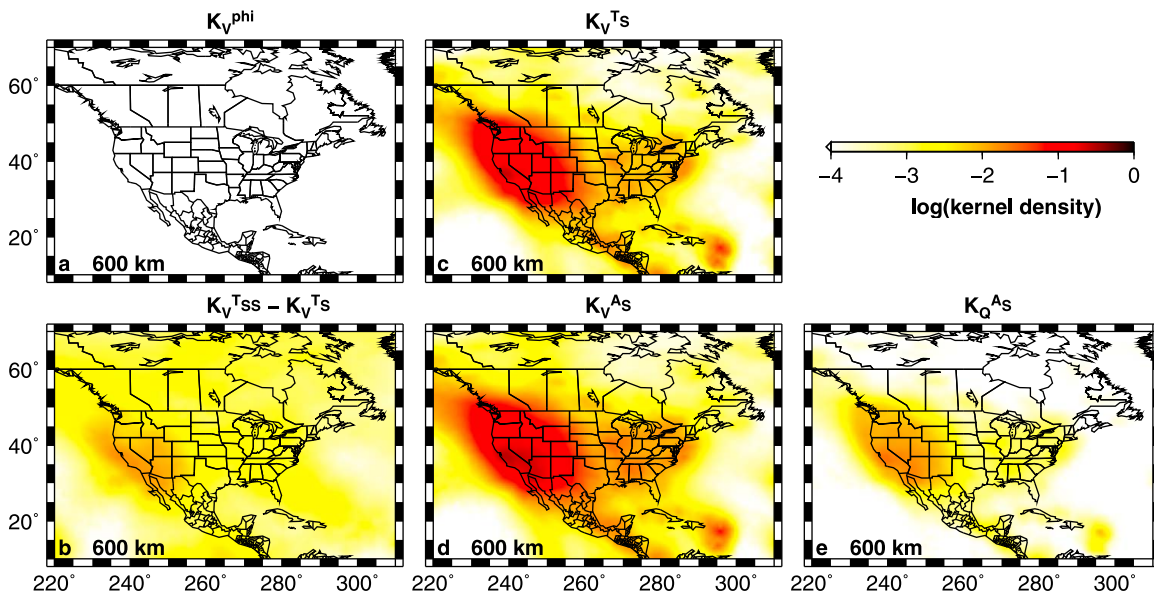


**Figure 6.** The kernel density (see equation (9)) for the five sensitivity kernels in equation (8) at 600 km depth. The heading indicates the kernel type. (a) For Love wave kernels and (b) for  $SS$  wave kernels. (c and d) For  $SH$  wave velocity kernels. (e) For  $SH$  wave attenuation kernels.

side, besides the velocity and attenuation heterogeneities, the model vector includes various correction terms:  $C^{TS}$  represents hypocenter and origin time corrections for  $SH$  wave traveltimes (see equation (4));  $C^{AS}$  represents receiver and source corrections for  $SH$  wave amplitudes (see equation (5));  $C^\phi$  represents origin time corrections for Love wave phase delays (see equation (7)). The body wave finite frequency sensitivity kernels  $K_V^{Ts}$ ,  $K_V^{As}$ ,  $K_Q^{As}$ ,  $K_V^{Tss}$  are computed using the software by Tian *et al.* [2007a, 2007b]. The Love wave finite frequency sensitivity kernels  $K_V^\phi$  are computed using the software by Zhou *et al.* [2006].  $K_C^{Ts}$ ,  $K_C^{As}$ ,  $K_C^\phi$  are ad hoc matrices for corrections  $C^{TS}$ ,  $C^{AS}$ ,  $C^\phi$  (see equations (4), (5), and (7)).  $W$  is a diagonal weighting matrix, with its diagonal element proportional to the tetrahedral volume associated with the corresponding grid point, and  $\epsilon_1$  is the norm damping parameter.  $R$  is the Laplacian roughening operator [Nolet, 2008, section 14.5], and  $\epsilon_2$  is the smoothing parameter. Equation (8) shows that velocity and attenuation have coupled effects on  $SH$  wave amplitudes, and  $SS$  and Love waves provide extra independent constraints on velocity. Our joint inversion interprets these data simultaneously.

[22] As a measure of how strongly a particular tetrahedral volume in the Earth is sensed by the combined set of kernels, we compute the “kernel density,” defined as

$$D_j = \frac{\sum_i K_{ij}}{CV_j}, \quad (9)$$

where  $K$  stands for the tomographic matrices in equation (8), summation  $i$  is over all data,  $V_j$  is the average volume of the tetrahedron containing grid point  $j$ , and  $C$  is a scaling constant such that the maximum  $D_j$  is 1. The factor  $1/V_j$  removes the effect of nonuniform grid spacing. Figures 5 and 6 plot  $\log(D_j)$  for all the five sensitivity kernels in equation (8), at 100 and 600 km depth, respectively. Figures 5c–5e and 6c–6e show the kernel densities for  $SH$  waves. The

dense coverage of the USArray is reflected in the large values of  $SH$  wave kernel densities in the western United States. For  $SH$  wave amplitudes, with the same ray coverage, the sensitivity to attenuation is about 1.5 orders of magnitude weaker than that to velocity. As we go deeper, the body wave sensitivity becomes wider although the strength slightly decreases near the geometrical rays. Figures 5a and 6a show that Love wave sensitivity is concentrated near the surface. Love and  $SS$  waves provide constraints on  $SH$  velocity outside of the U.S. region, where  $SH$  waves have poor coverage. Within the U.S. region, the Love wave and  $SS$  wave sensitivity is at least 1 order of magnitude smaller than that of  $SH$  waves, because of the small number of measurements for Love and  $SS$  waves. Nonetheless, they provide extra constraints independent of  $SH$  waves: Love waves are more sensitive to vertical gradients in velocity than  $SH$  waves.

### 3.3. The Inversion Scheme

[23] The joint linear system (8) has four different types of data with different orders of magnitude. Following a Bayesian philosophy [Nolet, 2008, section 14.5], we scale the data with their estimated measurement uncertainties (see section 2.4) and scale the model parameters with their “prior uncertainties,” which are estimated from results of existing tomographic studies. The model parameter prior uncertainties used in the final inversion are 0.01 for  $\delta \ln V_S$ , 0.2 for  $\delta \ln Q_S$ , 30 km for  $SH$  wave hypocenter corrections, 1 s for  $SH$  wave origin time corrections, 0.1 for  $SH$  wave amplitude event corrections, 0.15 for  $SH$  wave amplitude station corrections, and 1 s for phase delay origin time corrections. These estimates of both data and model uncertainties carry a subjective uncertainty and were in effect slightly adjusted within their margin of error as we gained experience with the data compatibilities during early inversion runs. Before inversion, the data and model parameters in equation (8) are divided by their uncertainties, and

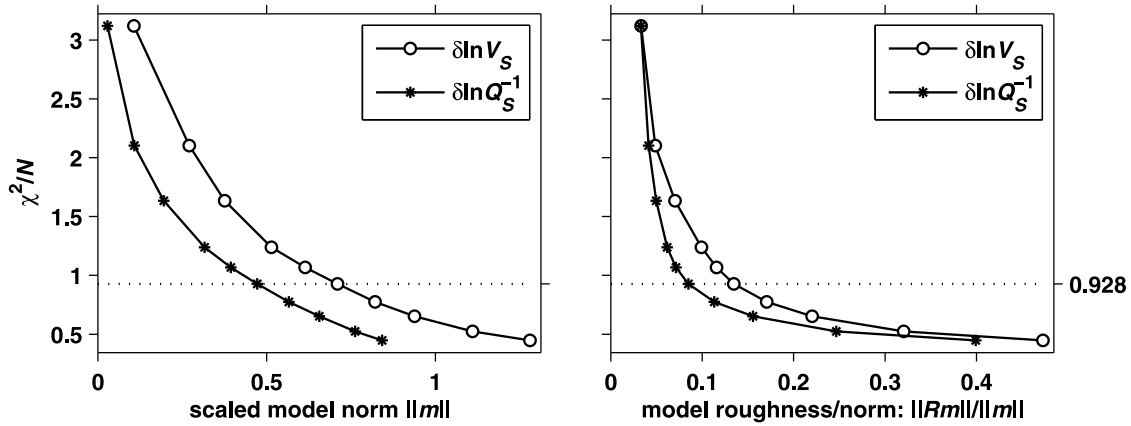


**Figure 7.** Trade-off curve for velocity (circles) and attenuation (asterisks) models. (left) Trade-off between fitting the data and norm damping. (right) Trade-off between fitting the data and smoothing the model. The term  $\chi^2/N$  is defined by equation (10),  $\mathbf{m}$  is the model vector  $\delta \ln V_S$  or  $\delta \ln Q_S^{-1}$  in equation (8),  $\mathbf{R}$  is the Laplacian roughening operator [Nolet, 2008, section 14.5], and verticals represent the L2 norm. Different points on the same curve correspond to different values of  $\epsilon_1$  or  $\epsilon_2$  in equation (8). The dotted line indicates the preferred model with  $\chi^2/N = 0.928$ .

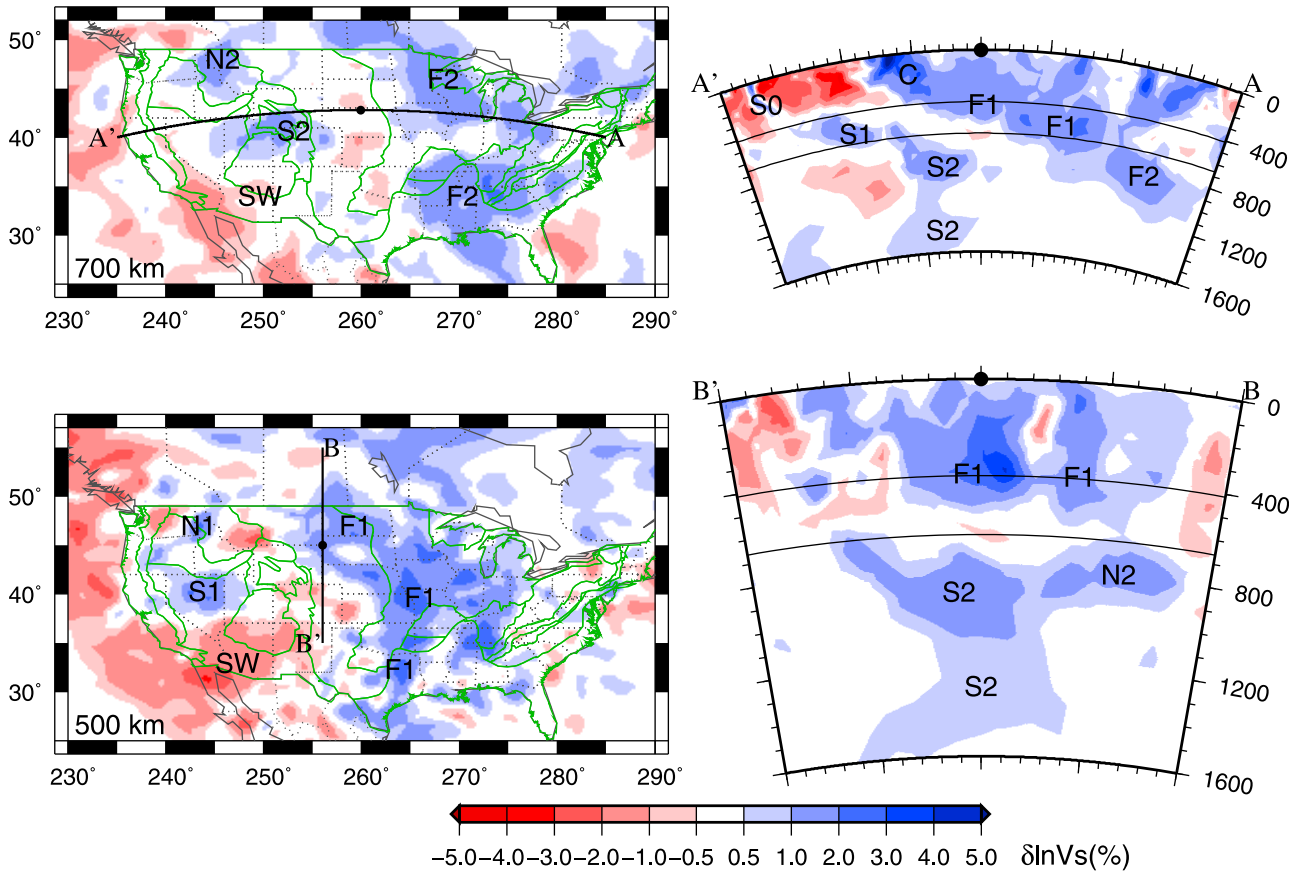


**Figure 8.** Great circle cross sections of the subduction system under North America. The black dot and  $0^\circ$  represent the midpoint of the great circle arc. In the map views, green lines delineate tectonic boundaries, dotted black lines delineate political boundaries, and the depth is indicated at the bottom left corner. In the cross-section views, the 410 km and 660 km discontinuities are indicated, and each grid along the arc represents  $1^\circ$ . SW denotes the slab window south of the Mendocino Fracture Zone, where no subduction exists. Cross section AA' shows the two separate subduction systems: the younger one in the west (S0, S1, S2) and the older one in the east (F1, F2); C denotes the craton. Cross section BB' shows that F1 lies above S2 and N2. Labels S1, N1, S2, N2, F1, F2 identify the same structure as in the work by Sigloch *et al.* [2008].

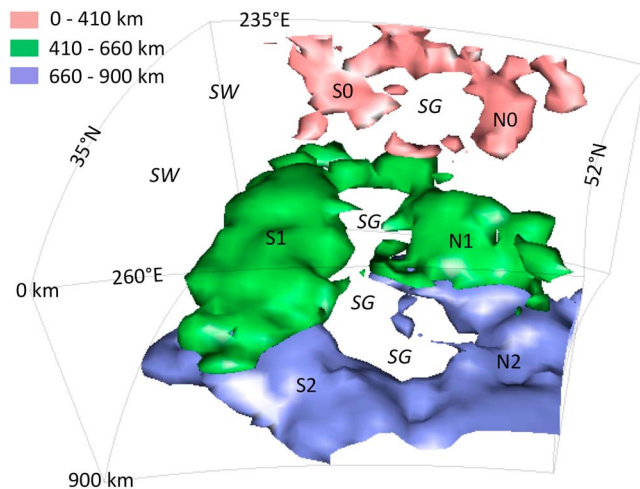


**Figure 9.** Three-dimensional view of the subduction system under the western United States, looking from the east. Plotted is the isosurface of  $\delta \ln V_S = +0.6\%$ . The extent and geometry of the structure only change modestly as we shift the contour level between 0.5% and 0.8%. Red represents the subduction in the upper mantle (S0, N0), green represents the subduction in the transition zone (S1, N1), and purple represents the subduction in the lower mantle (S2, N2). Fast anomalies that are not deemed to be subducted material (e.g., the craton, the Colorado Plateau root) are not displayed. SG represents the slab gap, which is a continuous trail void of fast anomalies and divides the slab into the northern part (N0, N1, N2) and the southern part (S0, S1, S2). SW denotes the slab window south of the Mendocino Fracture Zone, where no subduction exists. Labels S1, N1, S2, N2, SG identify the same structure as in the work by *Sigloch et al.* [2008].

the kernel matrices (all the  $\mathbf{K}$  in equation (8)) are scaled correspondingly.

[24] We expect a high resolution beneath the dense USArray but have meshed the entire globe in order to absorb delays or focusing effects acquired along wave paths outside of North America. No unique solution exists, and the linear system (8) is necessarily regularized. Our aim is for a model which interprets the data within their margin of uncertainties (satisfying rows 1–4 of (8)), while staying close to the reference model (satisfying rows 5–9 of (8)), and remaining as smooth as possible (satisfying rows 10–11 of (8)). This trade-off between fitting the data and regularizing the model is controlled by  $\epsilon_1$  and  $\epsilon_2$ . The scaled and regularized linear system (8) is solved by a parallel version of LSQR [*Paige and Saunders, 1982; Nolet, 1987*] on a cluster. Outliers with residuals larger than three standard deviations after a first run with negligible norm damping and smoothing are removed.

[25] In order to quantitatively assess the trade-off between fitting the data and regularization, we use  $\chi^2/N$  as a measure for the misfit of the observed data to the values predicted by finite frequency theory:

$$\frac{\chi^2}{N} = \frac{1}{N} \sum_{i=1}^N \left( \frac{d_i - \sum_j K_{ij} m_j}{\sigma_i} \right)^2, \quad (10)$$

where the summation over  $i$  is over the first four matrix rows in (8),  $K_{ij}$  is the submatrix formed by those rows,  $\sigma_i$  is the estimated uncertainty of datum  $d_i$ , and  $N$  is the total number of data. If  $\sigma_i$  is correctly estimated,  $\chi^2/N$  should be close to 1 for a model that fits the data, but which is not forced to fit the data closer than one standard deviation on average. Meanwhile, we use the L2 norm of the model vector  $\|\mathbf{m}\|$  as a measure for the deviation from the reference model and use the L2 norm ratio  $\|\mathbf{R}\mathbf{m}\|/\|\mathbf{m}\|$  as a measure for the roughness of the model, where  $\mathbf{m}$  is the model vector,  $\delta \ln V_S$  or  $\delta \ln Q_S^{-1}$  in equation (8), and  $\mathbf{R}$  is the Laplacian roughening operator [*Nolet, 2008, section 14.5*]. Figure 7 shows the trade-off between fitting the data and regularizing the model for velocity and attenuation, respectively. The preferred model has  $\chi^2/N = 0.928$  and is near the corner of the trade-off curves. The norms of the scaled  $\delta \ln V_S$  and  $\delta \ln Q_S^{-1}$  are of the same order, suggesting that the estimates for prior uncertainties in velocity and attenuation are reasonable.

## 4. The SH Velocity Model of the Mantle Beneath North America

[26] In this section, we discuss several interesting features of our SH velocity model of the mantle, which is the deviation from the IASP91 S velocity model [*Kennett and Engdahl, 1991*]. A complete catalog of the velocity maps is given in the auxiliary material in Figures S4–S6 (right).<sup>1</sup>

### 4.1. Subduction

[27] The fast velocity anomalies in our model confirms the two-stage subduction under North America and the existence of tears in the Farallon slab observed by *Sigloch et al.* [2008]. Figure 8 shows the whole subduction system under North America. Figures 9 and 10 show the subduction under the western United States and the tearing of the slab. To facilitate comparison with the earlier P wave inversions, we use the same notation (S1, N1, S2, N2, F1, F2, SG) as *Sigloch et al.* [2008] to identify anomalies.

[28] Fast anomalies are observed at 100–200 km depth under the Cascades (Figure S4, right; S0, N0 in Figures 9 and 10), indicating the most recently subducted Juan de Fuca Plate. It is subducting at a steep angle (S0 in Figure 8, AA'). The Juan de Fuca slab continues eastward, penetrating the transition zone (S1, N1 in Figures 8–10) and reaching the lower mantle (S2, N2 in Figures 8 and 9). Under the western United States down to ~800 km depth, no large fast anomaly is observed south of ~37°N (SW in Figures 8–10), which is the present Mendocino edge of the Juan de Fuca slab. This region with absence of subduction is known as the slab window, produced by the breakup and movement of the Farallon slab in the last ~28 Myr [*Atwater and Stock, 1998*]. Although *Schmandt and Humphreys* [2010a] found small-scale high-velocity anomalies possibly representing the slab coming to rest in the transition zone, our tomographic image indicates that the last large (~600 km) piece of the Farallon plate south of the Mendocino Triple Junction has sunk to at least 900 km depth. If the slab window formed at ~28 Ma [*Atwater and Stock, 1998*], this implies a vertical sinking

<sup>1</sup>Auxiliary materials are available in the HTML. doi:10.1029/2010JB007704.

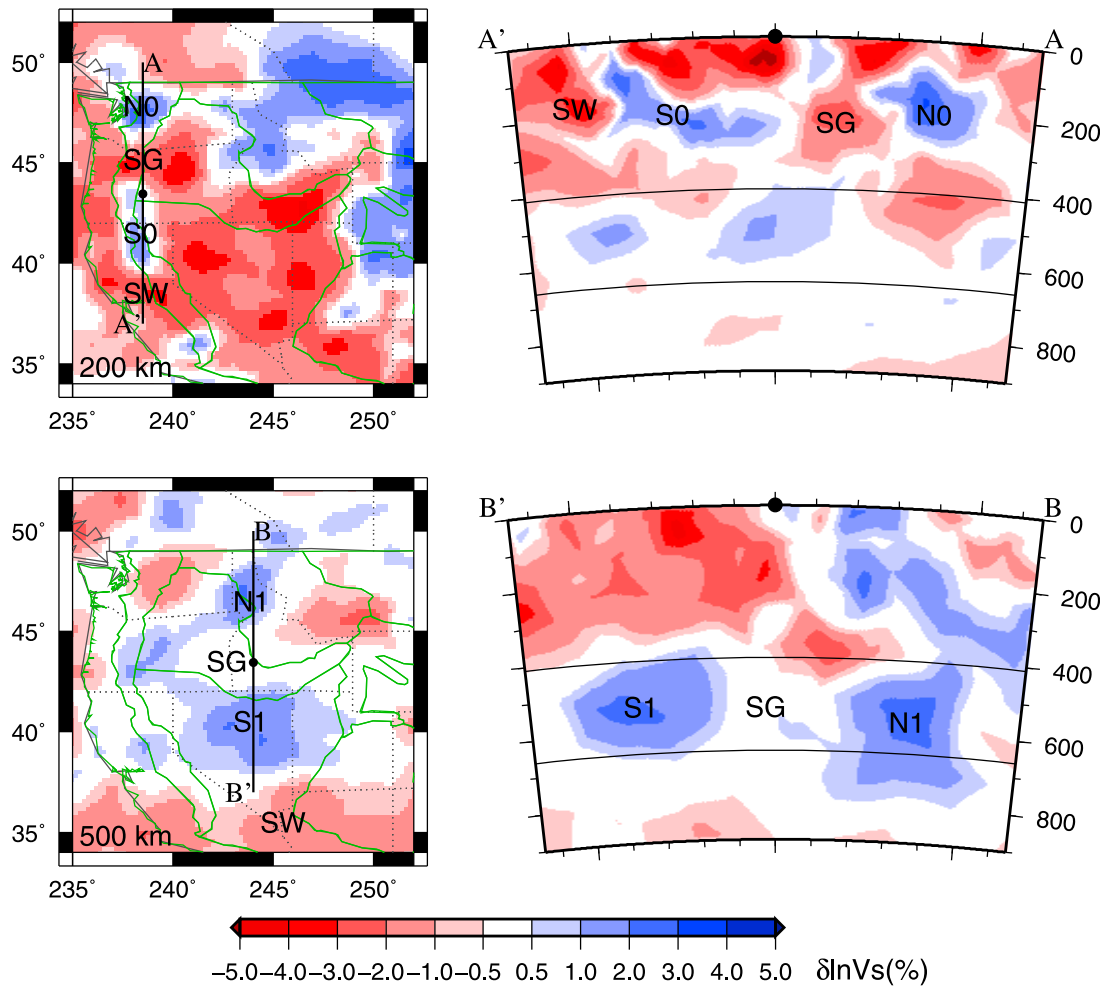


**Figure 10.** Great circle cross sections of the subduction system under the western United States. The black dot and  $0^\circ$  represent the midpoint of the great circle arc. In the map views, green lines delineate tectonic boundaries, dotted black lines delineate political boundaries, and the depth is indicated at the bottom left corner. In the cross-section views, the 410 km and 660 km discontinuities are indicated, and each grid along the arc represents  $1^\circ$ . SW denotes the slab window south of the Mendocino Fracture Zone, where no subduction exists. Cross section AA' goes through the subducted slab (S0, N0) and the slab gap (SG) in the upper mantle. Cross section BB' goes through the subducted slab (S1, N1) and the slab gap (SG) in the transition zone. Labels S1, N1, SG identify the same structure as in the work by *Sigloch et al.* [2008].

rate of 3.2 cm/yr, which is comparable to the speed of the Farallon plate at  $\sim 28$  Ma [Engebretson *et al.*, 1985].

[29] Under eastern North America, large volumes of fast anomalies (Figures S5 and S6, right; F1, F2 in Figure 8) are observed parallel to the young Juan de Fuca slab described above. They extend as far south as at least  $25^\circ\text{N}$ , occupying the mantle beneath eastern North America down to at least 1400 km. This probably represents the ancient Farallon slab, and it is well separated from the Juan de Fuca slab, as can be seen from Figure 8: the western tip of F1 is riding above the eastern tips of S2 and N2 with a gap in between. The coexistence of the western and eastern subduction systems was first observed by *Sigloch et al.* [2008] and interpreted in terms of a big break at 50–40 Ma between F1 and S1. Consistent with their  $V_p$  model, we observe a flat F1 in the transition zone (Figure 8, AA') and a relatively steeper

subduction angle of S1, which makes it easier for S1 to penetrate the transition zone.

[30] Taking advantage of the dense USArray coverage, we are able to obtain a high resolution under the western United States and thus to study the detailed structure of the Juan de Fuca slab. The most striking feature is the slab gap (SG in Figures 9 and 10), which is a continuous 1600 km long trail void of fast anomalies and which divides the Juan de Fuca slab into a northern part (N0, N1, N2) and a southern part (S0, S1, S2). It starts at  $\sim 120$  km depth near ( $45^\circ\text{N}$ ,  $238^\circ\text{E}$ ), extends northeastward as it sinks deeper, and ends at  $\sim 800$  km depth near ( $47^\circ\text{N}$ ,  $254^\circ\text{E}$ ) (Figure S5, right, 800 km). Because there is no surface evidence showing the absence of subduction near ( $45^\circ\text{N}$ ,  $238^\circ\text{E}$ ), the slab gap is more likely to have formed at  $\sim 120$  km depth rather than at surface. We exclude the kinematic segmentation of the monolithic Farallon plate starting at  $\sim 30$  Ma as the cause of the slab gap.

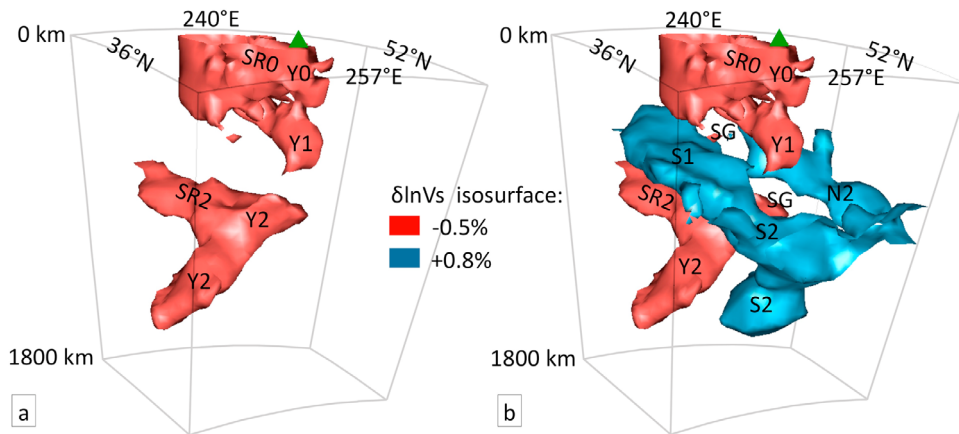


**Figure 11.** Three-dimensional view of the plume-slab interaction system under Yellowstone and the eastern Snake River Plain, looking from the southwest. Red represents the isosurface of slow anomalies  $\delta \ln V_S = -0.5\%$ , and blue represents the isosurface of fast anomalies  $\delta \ln V_S = +0.8\%$ . The extent and geometry of the structure only change modestly as we shift the contour level between 0.5% and 0.8%. The green triangle represents the location of the Yellowstone Caldera. For slow anomalies above 660 km, only those under Yellowstone and the eastern Snake River Plain ( $40\text{--}46^\circ\text{N}$ ,  $244\text{--}251^\circ\text{E}$ ) are displayed. Shallow fast anomalies that are not deemed to be subduction (e.g., the craton and the Colorado Plateau root) are not displayed. (a) Slow anomalies only. Under the eastern Snake River Plain, SR0 is in the upper mantle and SR2 is in the lower mantle. Under the Yellowstone Caldera, Y0 is in the upper mantle, Y1 is in the transition zone, and Y2 is in the lower mantle. (b) Superimposition of the fast anomalies on top of the slow anomalies. See Figure 9 for a description of the fast anomalies. Labels S1, N1, S2, N2, SG identify the same structure as in the work by *Sigloch et al.* [2008].

Most of this breakup of the Farallon plate occurred south of the Mendocino fracture zone, and the plate to the north (the Juan de Fuca plate) remained relatively intact [Atwater and Stock, 1998]. The slab gap revealed by our velocity model is inside the Juan de Fuca plate, so it is less likely to relate to the breakup of the monolithic Farallon plate. In addition, the slab gap reaches only 800 km depth, which suggests that the slab gap is younger than 30 Myr using the Farallon plate velocity by *Engebretson et al.* [1985]. One possible cause of the slab gap could be the different subduction angles of the northern and southern parts of the Juan de Fuca plate, as shown in Figure 9, S1 enters the transition zone at a further east location than N1. Our velocity model shows that the subduction angle is  $\sim 60^\circ$  (from surface) for S1, and  $\sim 70^\circ$  for N1, and the thickness of S1 and N1 is  $\sim 70$  km. A back-of-the-envelope calculation with this geometry suggests that S1 and N1 start to diverge (no overlap) at  $\sim 350$  km, which is much deeper than the observed 120 km depth. This indicates that there are other causes contributing to the formation of the slab gap in the meantime, such as the interaction between the Yellowstone plume and the slab [Obrebski et al., 2010]. This slab gap was first discovered by *Sigloch et al.* [2008]. In their  $P$  velocity model, the slab gap extends longer (2500 km long) and deeper (1200 km deep) than in our model. The slab gap is also recognizable in other recent tomographic models [e.g., *Obrebski et al.*, 2010; *Schmandt and Humphreys*, 2010b], although it is not discussed in these studies. The slab hole at shallow depth near  $45^\circ\text{N}$  under the Cascades that was observed in several recent studies [Roth et al., 2008; Tian et al., 2009; Burdick et al., 2009; *Schmandt and Humphreys*, 2010b] overlaps the upper tip of the slab gap, and thus is actually the top part of the slab gap.

[31] Evidence for more breaks or detachment of the slab is observed. At 700–1200 km depth, F2 is divided into two blob-like segments, along an east-west oriented break near  $\sim 40^\circ\text{N}$  (Figure 8, AA', and Figures S5 and S6, right). The  $V_P$  model [Sigloch et al., 2008] shows a break at similar location and depth, but extending broader in the north-south direction and shorter in the east-west direction than in our  $V_S$  model. S2 has a blob-like tail down to  $\sim 1600$  km depth (Figure 8). Blob-like slabs in the lower mantle are also observed by seismic tomography under northern Kuril and Mariana [Fukao et al., 2009]. Such droplet-like slabs are modeled by numerical simulation with a large viscosity contrast across the 660 km discontinuity [Tagawa, 2007]. The droplet-like shape suggests strong deformation and perhaps detachment of the slab as it penetrates the 660 km discontinuity. The discontinuity between S0(N0) and S1 (N1) (Figures 8, AA', and 9) is the evidence of a further small-scale tear in the Juan de Fuca slab.

[32] Different hypotheses explaining the Farallon slab segmentation have been proposed to explain the post-Laramide magmatism in the western United States. The “slab buckling” model [Humphreys, 1995] predicts east-west oriented Farallon slab remnants. Anomalies S1 at  $\sim 40^\circ\text{N}$  and N1 at  $\sim 47^\circ\text{N}$  cannot be the north and south sides of the buckle which is now near  $36^\circ\text{N}$ . The “slab roll back and detachment” model [van der Lee and Nolet, 1997a] and the “two-stage subduction” model [Sigloch et al., 2008] predict north-south oriented Farallon slab remnants. Our  $SH$  velocity model largely satisfies predictions from the subduction history of the Farallon slab proposed by *Sigloch et al.* [2008], such as the separation between anomalies S1 and F1, possibly resulting from a two stage subduction. Meanwhile we observe blob-like slab segments in the lower

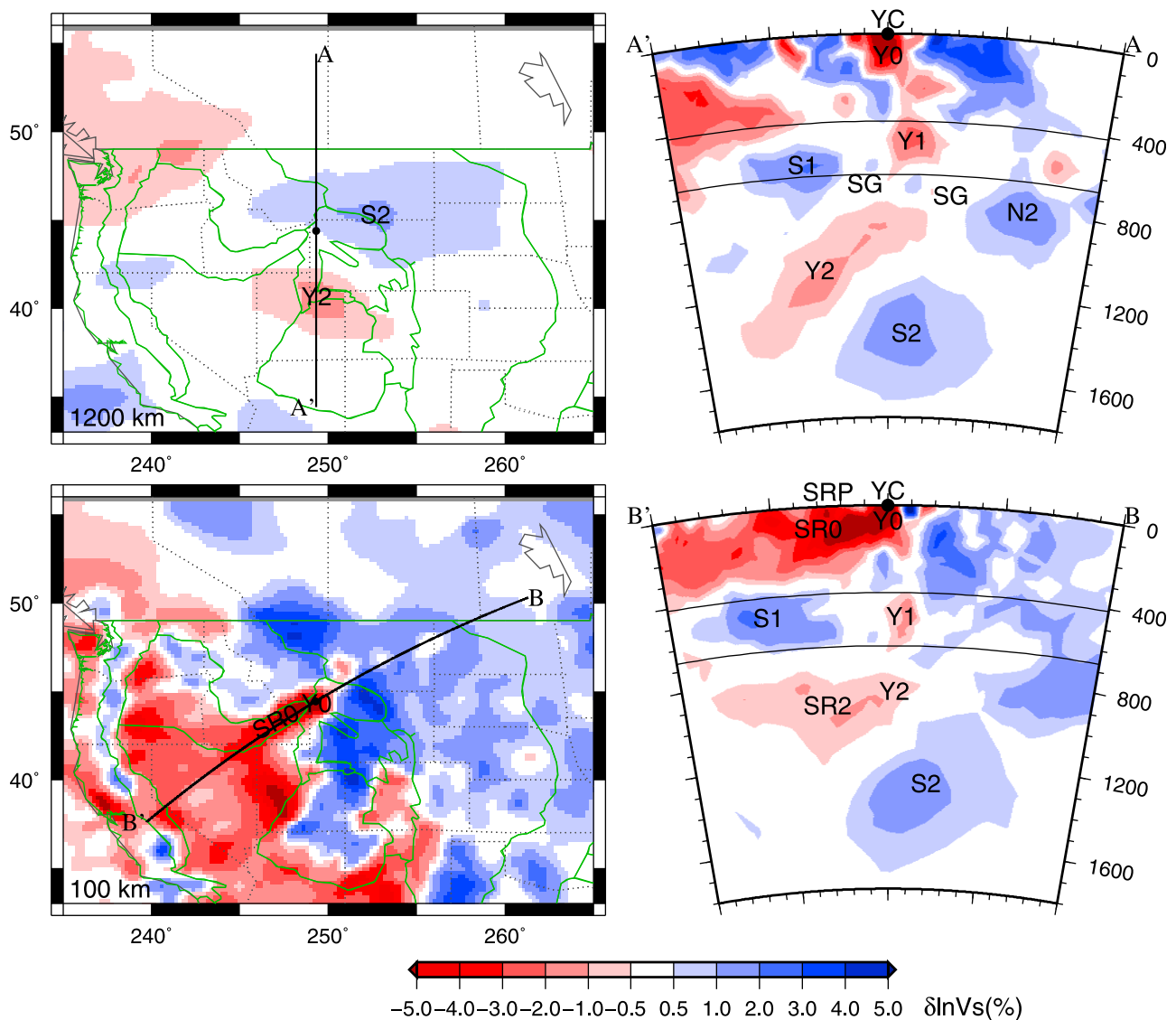


**Figure 12.** Great circle cross sections of the velocity structure under the Yellowstone Caldera (YC) and the eastern Snake River Plain (SRP). The black dot and 0° represent the location of the Yellowstone Caldera and the midpoint of the great circle arc. In the map views, green lines delineate tectonic boundaries, dotted black lines delineate political boundaries, and the depth is indicated at the bottom left corner. In the cross-section views, the 410 km and 660 km discontinuities are indicated, and each grid along the arc represents 1°. Cross section AA' goes through the Yellowstone plume trail (Y2, Y1, Y0). Cross section BB' goes through the eastern Snake River Plain (SRP) and the slow anomaly beneath it (SR2) and the northern edge of the Yellowstone plume trail (Y2, Y1, Y0). S1, S2, N2, SG are parts of the subduction system under the western United States (see Figure 9), and they identify the same structure as in the work by Sigloch *et al.* [2008].

mantle and other smaller-scale slab tears, all indicating high-level segmentation of the Farallon slab.

[33] The subduction-related features discussed above are reasonably well resolved, including the subduction under the Cascades (Figure S7, 100–200 km), the slab window (Figure S7, 100–800 km), the coexisting two subduction systems (Figure S8, AA'), the slab gap under the western United States (Figure S7, 200–800 km, and Figure S8, BB'), the break in F2 (Figure S7, 800–1200 km), the droplet-like geometry of S2 and F2 (Figure S8, AA'), and the discontinuity between S0 and S1 (Figure S8, AA').

#### 4.2. The Yellowstone Plume

[34] A strong slow anomaly (Y0) with large velocity gradient is observed under the Yellowstone Caldera (Figures 11a and 12). It has a diameter of ~200 km and reaches 200 km depth. Y0 connects to a 200 km wide slow anomaly (Y1) in the transition zone, which is centered at ~1° north of Y0 (Figure 12, AA'). To the southwest, Y0 abuts a belt of strong slow anomalies (SR0) under the eastern Snake River Plain (Figures 11a and 12, BB'). Down in the lower mantle, a plume-shaped 300 km wide conduit

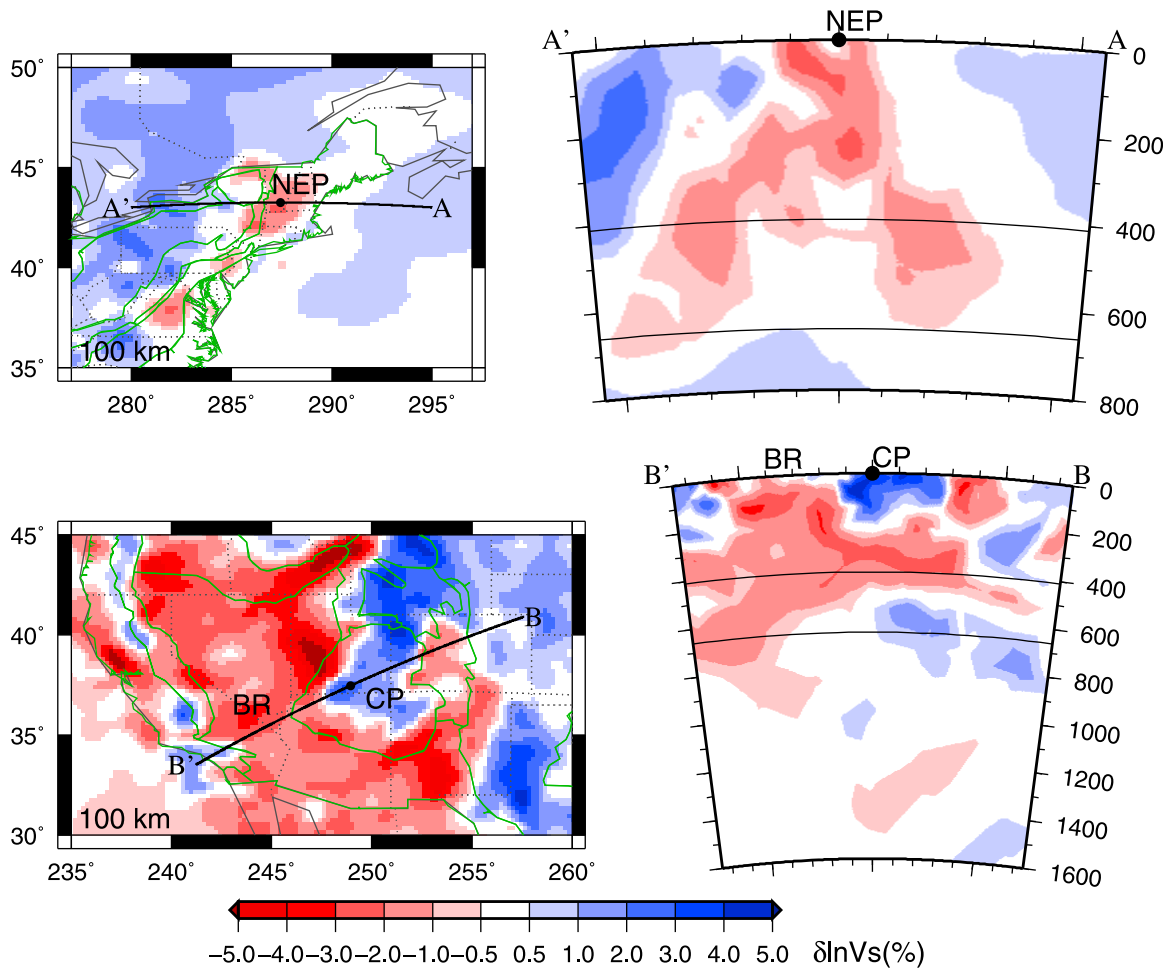


**Figure 13.** Great circle cross sections of selected small-scale velocity features. The black dot and  $0^\circ$  represent the midpoint of the great circle arc. In the map views, green lines delineate tectonic boundaries, dotted black lines delineate political boundaries, and the depth is indicated at the bottom left corner. In the cross-section views, the 410 km and 660 km discontinuities are indicated, and each grid along the arc represents  $1^\circ$ . Cross section AA' goes through slow anomalies under the New England Province (NEP). Cross section BB' goes through the Colorado Plateau (CP) and the Basin and Range (BR).

(Y2) is observed with its top directly under Y1. The plume comes from south, tilting  $\sim 40^\circ$  from vertical, reaches as deep as 1500 km, but spreads out at 700–1100 km depth. Figure S8, CC'–DD', shows that these velocity features are well resolved. A tilting plume under the Yellowstone that extends to the lower mantle is also observed by *Obrebski et al.* [2010] and *Schmandt and Humphreys* [2010b], but the plume comes from southwest in their models. The  $V_S$  model of *Obrebski et al.* [2010] also shows that the plume spreads out at 600–900 km depth, a feature quite similar to that in our model. The image of a tilting whole mantle plume is quite different from previous tomographic images, especially in the lower mantle. Regional studies have shown an upper mantle plume from northwest with a smaller tilting angle [*Yuan and Dueker*, 2005; *Waite et al.*, 2006], and other studies have revealed no plume-like features in the lower mantle [*Montelli et al.*, 2006; *Sigloch et al.*, 2008; *Burdick et al.*, 2009].

[35] The dimensions of Y0, Y1, and Y2 agree well with the expected plume radius from other studies [e.g., *Montelli*

*et al.*, 2004; *Steinberger and Antretter*, 2006]. The large southward tilting angle of Y2 is surprising because it would require a very strong mantle wind. Both *Steinberger and O'Connell* [1998] and *Steinberger* [2000] predict indeed a southward flow in the midmantle beneath the Yellowstone from numerical modeling of mantle flow. The spreading of SR2 can be explained either if the 660 km discontinuity acts as a barrier, as is sometimes observed for plumes [*Nolet et al.*, 2006], or if the slab fragment S1 acts as a barrier for the uprising Y2 (Figure 11b). Y2 might have distorted in two ways in response to the barrier. Part of Y2 might have navigated its path around S1 and found its way up through the slab gap, and the other part of Y2 might have smeared southwestward along the base of S1 and formed SR2. Though much of this explanation is speculative, it is clear that we witness a complex interaction between upwellings and downwellings in this part of the mantle.

[36] Much of Y0 and the eastern edge of SR0 have  $\delta \ln V_S < -5\%$  above 120 km (Figure 12, BB'), and the peak anomaly is  $-7\%$  at  $\sim 50$  km depth directly under the Yel-

lowstone Caldera. According to *Cammarano et al.* [2003] and *Goes and Govers* [2000],  $\delta \ln V_S < -5\%$  requires a thermal anomaly of  $\delta T > 250$  K, and the  $-7\%$  velocity anomaly under the caldera requires an  $\delta T$  of at least 350 K if it is a purely thermal effect. Tomographic studies with data from local transportable array experiments in the Yellowstone region [*Schutt et al.*, 2008; *Schmandt and Humphreys*, 2010b] show even slower velocities under the Yellowstone Caldera and the eastern Snake River Plain, which indicate even higher temperatures. These high temperatures reach the solidus of peridotite at 50–100 km depth [*Goes and van der Lee*, 2002], and thus may cause partial melt in these regions, especially under the caldera. The partial melt is probably responsible for the magmatism in the Yellowstone and eastern Snake River Plain.

#### 4.3. The New England Slow Anomaly

[37] Slow velocity anomalies up to  $-3\%$  are observed under the New England Province from the surface to the bottom of the transition zone (Figure 13, AA'), and they are well resolved (Figure S8, EE'). Low velocity in this region down to the transition zone has been reported by *van der Lee and Nolet* [1997b] and has been confirmed by recent body wave studies [*Sigloch*, 2008; *Burdick et al.*, 2009] and surface wave studies [*Bedle and van der Lee*, 2009]. According to *Cammarano et al.* [2003], under pure thermal effect, a  $-3\%$  velocity anomaly at 100 km depth and a  $-1\%$  velocity anomaly at 500 km depth require a thermal anomaly of at least 150 K and 220 K, respectively. This reaches the lower limit of the central temperature anomaly of an active mantle plume [e.g., *Nolet et al.*, 2006; *Steinberger and Antretter*, 2006]. On the other hand, the New England Province has been tectonically inactive for the last  $\sim 100$  Myr. The Montegesian hot spot passed through this region and created the Montegesian Hills at about 125 Ma [*Sleep*, 1990]. Hence, the thermal anomaly in this region should be weak at present, if not zero. Therefore, it is hard to explain the large amplitude of the velocity anomaly by a purely thermal effect. This suggests nonthermal origin of the observed slow velocity, possibly including both chemical heterogeneity and the presence of water/partial melt [*van der Lee et al.*, 2008].

#### 4.4. The Colorado Plateau

[38] The *SH* velocity model shows fast anomalies under the Colorado Plateau at 0–200 km depth (Figure 13, BB'). This high-velocity structure is thicker in the southwest than in the northeast, which is also observed by *P* wave tomography except with an overall thinner root [*Sigloch*, 2008]. This uneven thickness is resolved as shown in Figure S8, FF'. These fast anomalies probably represent a thick lithospheric root. Since the 2 km elevation of the Colorado Plateau largely exceeds the elevation that is expected to be supported by depleted cratonic lithosphere, some other form of support, static and/or dynamic, is needed. Various suggestions have been made, including warming of heterogeneous lithosphere [*Roy et al.*, 2009], edge-driven convection [*Karlstrom et al.*, 2008; *Van Wijk et al.*, 2010], dynamic modeling of mantle convection [*Moucha et al.*, 2009; *Liu and Gurnis*, 2010], and small-scale mantle convection represented by drip-like high-velocity bodies in tomographic images [*Schmandt and Humphreys*, 2010b]. In our *SH*

velocity model, we observe slow anomalies under southern California and northern Baja California in the lower mantle down to 1000 km depth. These slow anomalies overlap the warm mantle upwelling proposed by *Moucha et al.* [2009] which is responsible for the uplift in the central Basin and Range Province and Colorado Plateau. The thicker root in the southwest coincides with the higher accumulative dynamic topography in the southwest plateau for the last 25 Myr from the mantle convection model [*Moucha et al.*, 2009].

[39] In the upper mantle, at 100 km depth (Figure 13, BB', map view), anomalies as low as  $-6\%$  are observed under the boundary between the Colorado Plateau and the Basin and Range. The large magnitude of the slow anomalies suggest partial melt, as discussed in section 4.2, or the existence of water, which might be a result of hydration of the mantle beneath the Basin and Range due to the subduction of the Farallon slab under this region over 30 Myr ago [*Atwater and Stock*, 1998]. The slow anomaly rapidly changes to a fast anomaly as we go southeast from the Basin and Range to the Colorado Plateau, with a velocity contrast of  $9.0\%$  over 150 km. This large velocity gradient is resolved in our model as shown in Figure S7 (100 km). *Sine et al.* [2008] propose that this large velocity gradient defines a boundary between altered Paleozoic lithosphere (under the Basin and Range) and unaltered Proterozoic lithosphere (under the Colorado Plateau).

### 5. The Attenuation Model of the Mantle Beneath North America

[40] A catalog of the attenuation maps is given in Figures S4–S6 (left). These maps show that a large portion of the attenuation signal is located in the western United States, because the attenuation resolution in the central and eastern United States is low (Figure 12) due to poor data coverage (Figures 5e and 6e). Figure S9 shows that the attenuation resolution (especially amplitude recovery) starts to decrease at 600 km depth and the anomalies become unresolvable at 800 km depth and below. In the following, we discuss the relationship between attenuation and velocity anomalies in the upper mantle and transition zone beneath the United States, which may provide extra constraints on the physical sources of mantle heterogeneities.

[41] If we assume an approximate linear relationship  $\delta \ln Q_S = k \delta \ln V_S + b$ , then the correlation coefficient between  $\delta \ln Q_S$  and  $\delta \ln V_S$  describes the strength of this linear relationship. Because different physical sources (e.g., temperature, water content, partial melt, chemical composition, grain size) of mantle heterogeneities give different slopes of the linear relationship, a low correlation coefficient suggests coexistence of multiple physical sources. Even the same physical source has a depth-dependent property and thus produces a depth-dependent slope, so we study the correlation coefficient and slope at each depth rather than the average value. Figure 14a plots the variation of the signed correlation coefficient with depth for the western United States (WUS, west of  $255^\circ\text{E}$ ) and the central and eastern United States (EUS, east of  $255^\circ\text{E}$ ), respectively. All correlation coefficients are positive, meaning a dominant coexistence of slow (fast) velocity and high (low) attenuation. Such positive correlation is also observed in global

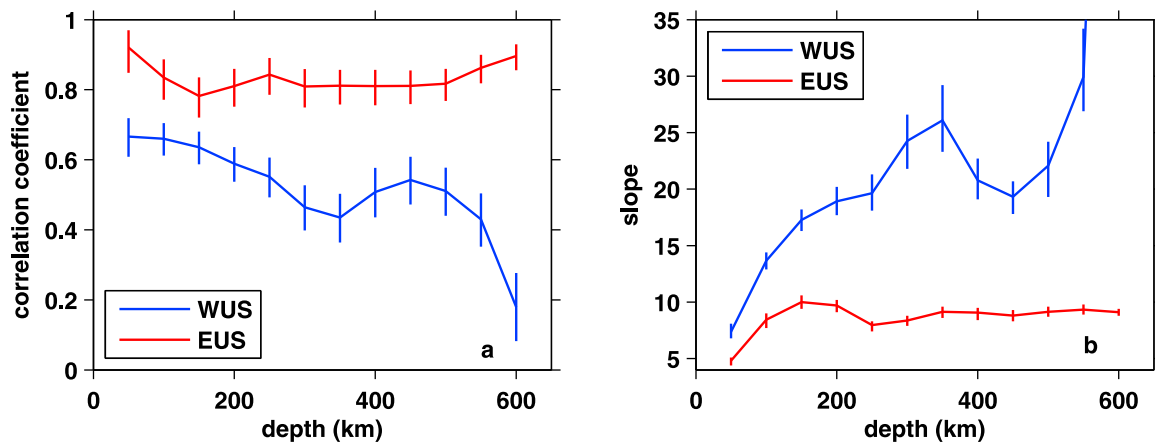


**Figure 14.** (a) Variation of signed correlation coefficient between  $\delta \ln V_S$  and  $\delta \ln Q_S$  with depth. The vertical bar represents the 95% confidence interval. (b) Variation of slope  $\partial(\delta \ln Q_S)/\partial(\delta \ln V_S)$  with depth. At each depth, the slope is estimated as the direction of the major axis of the error ellipse. The vertical bar gives the slope uncertainty, which is estimated with a 10% resampling technique (jackknifing [Tian et al., 2009]). The slope at 600 km depth under WUS is out of the axis range. In both Figures 14a and 14b, blue is for the western United States (WUS, west of 255°E) and red is for the central and eastern United States (EUS, east of 255°E). Points with  $|\delta \ln V_S| < 0.5\%$  or  $|\delta \ln Q_S| < 5\%$  are not used in producing the plots.

models derived from surface waves [e.g., Romanowicz, 1990; Artemieva et al., 2004; Dalton and Ekström, 2006] and in regional studies [e.g., Roth et al., 2000]. A positive correlation is predicted for the effects of most physical sources, such as temperature [e.g., Karato, 1993; Jackson et al., 2002], water content [e.g., Karato, 2006], partial melt with grain boundary sliding [e.g., Jackson et al., 2004; Faul et al., 2004], and grain size [e.g., Faul and Jackson, 2005]. The large correlation coefficient for EUS suggests one major physical source of attenuation and velocity heterogeneities under EUS, which is most likely temperature [e.g., Shito et al., 2006]. WUS has a lower correlation coefficient than EUS, suggesting that nonthermal sources play a more important role in forming heterogeneities under WUS, especially at the larger depth.

[42] Further insight into the physical state of the mantle comes from examining the variation of the slope  $k = \partial(\delta \ln Q_S)/\partial(\delta \ln V_S)$  with depth (Figure 14b). Because  $\delta \ln Q_S$  and  $\delta \ln V_S$  do not have a strict linear relationship, we treat them as random variables and estimate the slope as the direction of the major axis of the error ellipse. A formal estimate for the uncertainty in the slope is obtained using a 10% resampling technique (jackknifing [Tian et al., 2009]). Figure 14 shows that small slope uncertainties correspond to large correlation coefficients (e.g., under EUS), and this is expected from the situation of one major physical source. Large slope uncertainties correspond to small correlation coefficients (e.g., around 350 km depth under WUS), and are expected from the coexistence of multiple physical sources. The correlation coefficient at 600 km depth under WUS is so low that a simple linear relationship is no longer sufficient. Therefore we do not discuss the slope at this depth. The slope for EUS mainly reflects the behavior of thermal effects, as discussed above. The slope for WUS is significantly larger than that for EUS, suggesting nonthermal physical sources under WUS that produce larger slopes

than temperature, especially around 350 km depth. Such sources are possibly increasing water content [Karato, 2006] and partial melt with grain boundary sliding [Jackson et al., 2004; Faul et al., 2004].

[43] Extra constraints on the physical state of the mantle may be obtained by examining the lateral variation of the  $\delta \ln V_S - \delta \ln Q_S$  relationship. Figure 15 shows maps of the normalized  $C = \delta \ln V_S \times \delta \ln Q_S$  in the upper mantle and transition zone under North America. Positive values of  $C$  are dominant, consistent with the observed positive correlation coefficients (Figure 14a). Large-scale positive  $C$  exists in various tectonic regions, e.g., in the Wyoming craton at 100–200 km depth, under the magmatically active Basin and Range at 100–200 km depth, in the subducted slabs under Iowa, Illinois, Missouri at 400–600 km depth. Positive correlation under the old continents and magmatic regions on a global scale is reported by Dalton et al. [2009]. Note that large positive  $C$  does not necessarily indicate a large correlation coefficient, because there may be multiple physical sources with different (but all positive) slopes  $k$ , which in combination gives a relatively low (but positive) correlation coefficient. Relatively large-scale anticorrelation between  $\delta \ln V_S$  and  $\delta \ln Q_S$  (negative  $C$ ) is also observed, and one can only speculate about its cause. Low velocity and low attenuation coexist under the northwest coast at 200–400 km depth. This is likely due to the smearing of the slab-related, low-attenuation feature in the attenuation model. The coexistence of low velocity and low attenuation under the Central Valley at 100–400 km depth is more puzzling, though it may perhaps be explained by the effect of partial melt with a melt-squirt mechanism [Hammond and Humphreys, 2000a, 2000b]. A third example of anticorrelation is the coexistence of high velocity and high attenuation under the Northern Rocky Mountains at 100–200 km depth. Calculations show that for natural peridotites, an increase in Mg# significantly increases  $V_S$  [Lee, 2003]. On the other hand, attenuation is

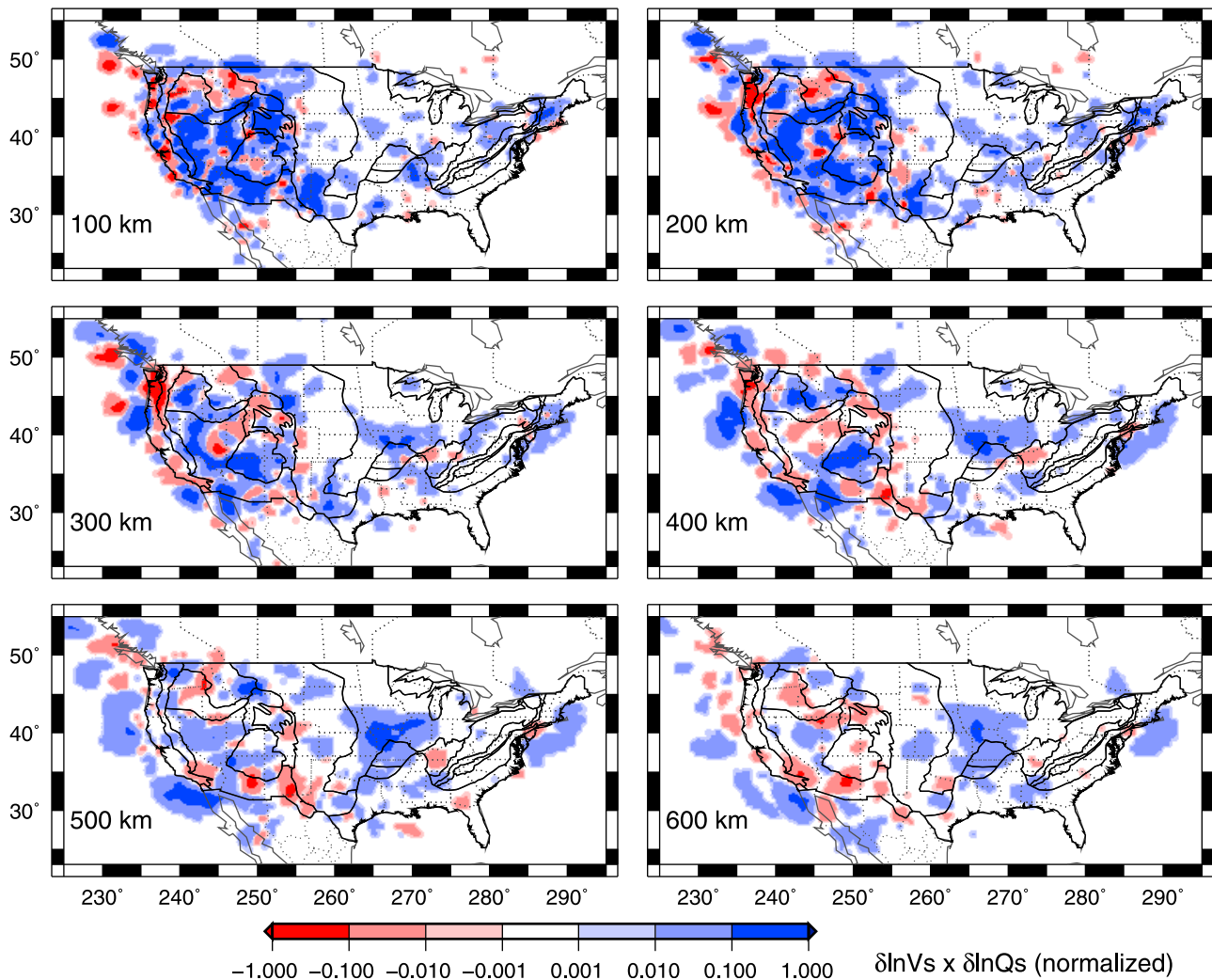


**Figure 15.** Maps showing  $\delta \ln V_S \times \delta \ln Q_S$  at 100–600 km depth. The value is normalized to have a maximum of 1. Points with  $|\delta \ln V_S| < 0.5\%$  or  $|\delta \ln Q_S| < 5\%$  are not used in producing the figure, in order to avoid that damping effects dominate the correlation.

expected to be much less sensitive to major element variations [Karato, 2006].

## 6. Conclusions

[44] We perform a joint inversion on multiple-frequency *SH* wave delays and amplitude anomalies, *SS* wave differential delays, and Love wave fundamental mode phase delays, to simultaneously obtain the velocity and attenuation structure under North America. Besides the intrinsic frequency dependence of Love wave phases, frequency dependence is also observed for all the body wave data in our study, indicating the presence of anomalies smaller than the width of the Fresnel zones.

[45] Our *SH* velocity model very much confirms the same fast anomalies as in the *P* velocity model by Sigloch *et al.* [2008], including the two separate subduction systems under North America and the slab gap under the western United States. It also reveals further evidence of high-level segmentation and deformation of the slab, including the droplet-like fragments of S2 and F2 in the lower mantle, a

tear in F2 under 700 km, and discontinuities around 410 km depth in the slab under the western United States. With the more recent USArray data, we are able to extend the high velocity resolution further east compared with Sigloch *et al.* [2008] and Tian *et al.* [2009], and start to see a glimpse of the Yellowstone plume. A lower mantle plume Y2 is observed to originate from about 1500 km depth and to rise up through the slab gap. We propose that a southward mantle flow produces the 40° tilting angle (from vertical) of Y2.

[46] Attenuation is only resolved in the upper mantle and transition zone under the United States. Large positive correlation coefficients between  $\delta \ln V_S$  and  $\delta \ln Q_S$  are observed under the central and eastern United States, suggesting one major physical source of mantle heterogeneities, most likely temperature. Smaller correlation coefficients and larger  $\delta \ln Q_S - \delta \ln V_S$  slopes are observed under the western United States, suggesting that nonthermal physical sources, probably the existence of water and partial melt (with grain boundary sliding), are playing a more important role, especially around 350 km depth. Anticorrelation is observed

in the upper mantle under the Central Valley and the Northern Rocky Mountains.

[47] The inclusion of Love wave phase delays helps improve velocity resolution in the lower mantle by better constraining the upper mantle. It also influences the attenuation image indirectly by changing the velocity image and thus the focusing effect, resulting in weaker attenuation anomalies above 200 km and stronger attenuation anomalies below 500 km. The misfits of Love wave and *SS* wave data are larger than those of *SH* wave data.

[48] **Acknowledgments.** We thank Frederik Simons, Nadine McQuarrie, Tom Duffy, and Eugene Humphreys for helpful discussions. Yue Tian was supported by the US National Science Foundation under grant numbers EAR-0309298 and EAR-0105387. Ying Zhou was supported by the US National Science Foundation under grant numbers EAR-0809464. Guust Nolet received support from the ERC (Advanced grant 226837) and a Marie Curie Re-integration grant (project 223799). Part of the maps are produced with GMT [Wessel and Smith, 1998].

## References

- Artemieva, I. M., M. Billien, J. J. L  v  que, and W. D. Mooney (2004), Shear wave velocity, seismic attenuation, and thermal structure of the continental upper mantle, *Geophys. J. Int.*, *157*, 607–628.
- Atwater, T., and J. Stock (1998), Pacific-North America plate tectonics of the Neogene southwestern United States: An update, *Int. Geol. Rev.*, *40*, 375–402.
- Bassin, C., G. Laske, and G. Masters (2000), The current limits of resolution for surface wave tomography in North America, *Eos Trans. AGU*, *81* (48), Fall Meet. Suppl., Abstract S12A-03.
- Bedle, H., and S. van der Lee (2009), *S* velocity variations beneath North America, *J. Geophys. Res.*, *114*, B07308, doi:10.1029/2008JB005949.
- Buehler, J. S., and P. M. Shearer (2010), Ph tomography of the western United States using USArray, *J. Geophys. Res.*, *115*, B09315, doi:10.1029/2009JB006874.
- Burdick, S., R. D. van der Hilst, F. L. Vernon, V. Marynov, T. Cox, J. Eakins, T. Mulder, L. Astiz, and G. L. Pavlis (2009), Model update December 2008: Upper mantle heterogeneity beneath North America from *P* wave travel time tomography with global and USArray transportable array data, *Seismol. Res. Lett.*, *80*, 638–644.
- Cammarano, F., S. Goes, P. Vacher, and D. Giardini (2003), Inferring upper-mantle temperatures from seismic velocities, *Phys. Earth Planet. Inter.*, *138*, 197–222.
- Dahlen, F. A., and A. M. Baig (2002), Fr  chet kernels for body wave amplitudes, *Geophys. J. Int.*, *150*, 440–466.
- Dahlen, F. A., S.-H. Hung, and G. Nolet (2000), Fr  chet kernels for finite-frequency traveltimes—I. Theory, *Geophys. J. Int.*, *141*, 157–174.
- Dalton, C. A., and G. Ekstr  m (2006), Global models of surface wave attenuation, *J. Geophys. Res.*, *111*, B05317, doi:10.1029/2005JB003997.
- Dalton, C. A., G. Ekstr  m, and A. M. Dziewonski (2009), Global seismological shear velocity and attenuation: A comparison with experimental observations, *Earth Planet. Sci. Lett.*, *284*, 65–75.
- Dziewonski, A. M., and D. L. Anderson (1981), Preliminary reference Earth model, *Phys. Earth Planet. Inter.*, *25*, 297–356.
- Engelbreton, D. C., A. Cox, and R. G. Gordon (1985), Relative motions between oceanic and continental plates in the Pacific basin, *Spec. Pap. Geol. Soc. Am.*, *206*, 59 pp.
- Faul, U. H., and I. Jackson (2005), The seismological signature of temperature and grain size variations in the upper mantle, *Earth Planet. Sci. Lett.*, *234*, 119–134.
- Faul, U. H., J. D. Fitz Gerald, and I. Jackson (2004), Shear wave attenuation and dispersion in melt-bearing olivine polycrystals: 2. Microstructural interpretation and seismological implications, *J. Geophys. Res.*, *109*, B06202, doi:10.1029/2003JB002407.
- Fukao, Y., M. Obayashi, T. Nakakuki, and the Deep slab Project Group (2009), Stagnant slabs: A review, *Annu. Rev. Earth Planet. Sci.*, *37*, 19–46.
- Gilbert, F., and A. M. Dziewonski (1975), An application of normal mode theory to the retrieval of structural parameters and source mechanisms from seismic spectra, *Philos. Trans. R. Soc. London, Ser. A*, *278*, 187–269.
- Goes, S., and R. Govers (2000), Shallow mantle temperatures under Europe from *P* and *S* wave tomography, *J. Geophys. Res.*, *105*, 11,153–11,169.
- Goes, S., and S. van der Lee (2002), Thermal structure of the North American uppermost mantle inferred from seismic tomography, *J. Geophys. Res.*, *107*(B3), 2050, doi:10.1029/2000JB000049.
- Goes, S., F. A. Capitanio, and G. Morra (2008), Evidence of lower-mantle slab penetration phases in plate motions, *Nature*, *451*, 981–984.
- Hammond, W. C., and E. D. Humphreys (2000a), Upper mantle seismic wave velocity: effects of realistic partial melt geometries, *J. Geophys. Res.*, *105*, 10,975–10,986.
- Hammond, W. C., and E. D. Humphreys (2000b), Upper mantle seismic wave attenuation: effects of realistic partial melt distribution, *J. Geophys. Res.*, *105*, 10,987–10,999.
- Humphreys, E. D. (1995), Post-Laramide removal of the Farallon slab, western United States, *Geology*, *23*, 987–990.
- Hwang, Y. K., J. Ritsema, and S. Goes (2009), Spatial variations of *P* wave attenuation in the mantle beneath North America, *J. Geophys. Res.*, *114*, B06312, doi:10.1029/2008JB006091.
- Jackson, I., J. D. Fitz Gerald, U. H. Faul, and B. H. Tan (2002), Grain-size-sensitive seismic wave attenuation in polycrystalline olivine, *J. Geophys. Res.*, *107*(B12), 2360, doi:10.1029/2001JB001225.
- Jackson, I., U. H. Faul, J. D. Fitz Gerald, and B. H. Tan (2004), Shear wave attenuation and dispersion in melt-bearing olivine polycrystals: 1. Specimen fabrication and mechanical testing, *J. Geophys. Res.*, *109*, B06201, doi:10.1029/2003JB002406.
- Karato, S.-I. (1993), Importance of anelasticity in the interpretation of seismic tomography, *Geophys. Res. Lett.*, *15*, 1623–1626.
- Karato, S.-I. (2006), Remote sensing of hydrogen in Earth’s mantle, in *Medical Mineralogy and Geochemistry*, *Rev. Mineral. Geochem.*, vol. 62, edited by N. Sahai and M. A. A. Schoonen, pp. 343–375, Mineral. Soc. of Am., Chantilly, Va.
- Karlstrom, K. E., R. Crow, L. J. Crossey, D. Coblenz, and J. W. Van Wijk (2008), Model for tectonically driven incision of the younger than 6 Ma Grand Canyon, *Geology*, *36*, 835–838, doi:10.1130/G25032A.
- Kennett, B. L. N., and E. R. Engdahl (1991), Traveltimes for global earthquake location and phase identification, *Geophys. J. Int.*, *105*, 429–465.
- Laske, G., and G. Masters (1996), Constraints on global phase velocity maps from long-period polarization data, *J. Geophys. Res.*, *101*, 16,059–16,075.
- Lawrence, J. F., P. M. Shearer, and G. Masters (2006), Mapping attenuation beneath North America using waveform cross-correlation and cluster analysis, *Geophys. Res. Lett.*, *33*, L07315, doi:10.1029/2006GL025813.
- Lee, C.-T. A. (2003), Compositional variation of density and seismic velocities in natural peridotites at STP conditions: Implications for seismic imaging of compositional heterogeneities in the upper mantle, *J. Geophys. Res.*, *108*(B9), 2441, doi:10.1029/2003JB002413.
- Liu, L., and M. Gurnis (2010), Dynamic subsidence and uplift of the Colorado Plateau, *Geology*, *38*, 663–666, doi:10.1130/G30624.1.
- Montelli, R., G. Nolet, F. A. Dahlen, G. Masters, E. R. Engdahl, and S.-H. Hung (2004), Global *P* and *PP* travel time tomography: Rays vs. waves, *Geophys. J. Int.*, *158*, 637–654.
- Montelli, R., G. Nolet, F. A. Dahlen, and G. Masters (2006), A catalogue of deep mantle plumes: New results from finite-frequency tomography, *Geochem. Geophys. Geosyst.*, *7*, Q11007, doi:10.1029/2006GC001248.
- Moucha, R., A. M. Forte, D. B. Rowley, J. X. Mitrovica, N. A. Simmons, and S. P. Grand (2009), Deep mantle forces and the uplift of the Colorado Plateau, *Geophys. Res. Lett.*, *36*, L19310, doi:10.1029/2009GL039778.
- Nolet, G. (1987), Seismic wave propagation and seismic tomography, in *Seismic Tomography*, edited by G. Nolet, pp. 1–23, D. Reidel, Dordrecht, Netherlands.
- Nolet, G. (2008), *A Breviary of Seismic Tomography*, Cambridge Univ. Press, Cambridge, U. K.
- Nolet, G. (2009), Slabs do not go gently, *Science*, *324*, 1152–1153.
- Nolet, G., and F. A. Dahlen (2000), Wave front healing and the evolution of seismic delay times, *J. Geophys. Res.*, *105*, 19,043–19,054.
- Nolet, G., S.-I. Karato, and R. Montelli (2006), Plume fluxes from seismic tomography, *Earth Planet. Sci. Lett.*, *248*, 685–699.
- Obayashi, M., D. Suetsugu, and Y. Fukao (2004), *PP*-*P* differential traveltime measurement with crustal correction, *Geophys. J. Int.*, *157*, 1152–1162.
- Obrebski, M., R. M. Allen, M. Xue, and S.-H. Hung (2010), Slab-plume interaction beneath the Pacific Northwest, *Geophys. Res. Lett.*, *37*, L14305, doi:10.1029/2010GL043489.
- Paige, C. C., and M. A. Saunders (1982), LSQR: An algorithm for sparse, linear equations and sparse least squares, *Trans. Math. Software*, *8*, 43–71.
- Paulssen, H., and E. Stutzmann (1996), On *PP*-*P* differential travel time measurements, *Geophys. Res. Lett.*, *14*, 1833–1836.
- Persson, P.-O., and G. Strang (2004), A simple mesh generator in Matlab, *SIAM Rev.*, *46*, 329–345.

- Reid, F. J. L., J. H. Woodhouse, and H. J. van Heijst (2001), Upper mantle attenuation and velocity structure from measurements of differential  $S$  phases, *Geophys. J. Int.*, *145*, 615–630.
- Ritsema, J., H. J. van Heijst, J. H. Woodhouse, and A. Deuss (2009), Long-period body wave traveltimes through the crust: Implications for crustal corrections and seismic tomography, *Geophys. J. Int.*, *179*, 1255–1261.
- Romanowicz, R. (1990), The upper mantle degree 2: Constraints and inferences from global mantle wave attenuation measurements, *J. Geophys. Res.*, *95*, 11,051–11,071.
- Roth, E. G., D. A. Wiens, and D. Zhao (2000), An empirical relationship between seismic attenuation and velocity anomalies in the upper mantle, *Geophys. Res. Lett.*, *27*, 601–604.
- Roth, J. B., M. J. Fouch, D. E. James, and R. W. Carlson (2008), Three-dimensional seismic velocity structure of the northwestern United States, *Geophys. Res. Lett.*, *35*, L15304, doi:10.1029/2008GL034669.
- Roy, M., T. H. Jordan, and J. Pederson (2009), Colorado Plateau magmatism and uplift by warming of heterogeneous lithosphere, *Nature*, *459*, 978–982.
- Schellart, W. P., J. Freeman, D. R. Stegman, L. Moresi, and D. May (2007), Evolution and diversity of subduction zones controlled by slab width, *Nature*, *446*, 308–311.
- Schmandt, B., and E. Humphreys (2010a), Seismic heterogeneity and small-scale convection in the southern California upper mantle, *Geochem. Geophys. Geosyst.*, *11*, Q05004, doi:10.1029/2010GC003042.
- Schmandt, B., and E. Humphreys (2010b), Complex subduction and small-scale convection revealed by body wave tomography of the western United States upper mantle, *Earth Planet. Sci. Lett.*, *297*, 435–445, doi:10.1016/j.epsl.2010.06.047.
- Schutt, D. L., K. Dueker, and H. Yuan (2008), Crust and upper mantle velocity structure of the Yellowstone hot spot and surroundings, *J. Geophys. Res.*, *113*, B03310, doi:10.1029/2007JB005109.
- Shito, A., S.-I. Karato, K. N. Matsukage, and Y. Nishihara (2006), Towards mapping the three-dimensional distribution of water in the upper mantle from velocity and attenuation tomography, in *Earth's Deep Water Cycle*, edited by S. D. Jacobsen and S. van der Lee, pp. 225–236, AGU, Washington, D. C.
- Sigloch, K. (2008), Multiple-frequency body wave tomography, Ph.D. thesis, 249 pp., Princeton Univ., Princeton, N. J.
- Sigloch, K., and G. Nolet (2006), Measuring finite-frequency body wave amplitudes and traveltimes, *Geophys. J. Int.*, *167*, 271–287.
- Sigloch, K., N. McQuarrie, and G. Nolet (2008), Two-stage subduction history under North America inferred from finite-frequency tomography, *Nat. Geosci.*, *1*, 458–462.
- Sine, C. R., D. Wilson, W. Gao, S. P. Grand, R. Aster, J. Ni, and W. S. Baldrige (2008), Mantle structure beneath the western edge of the Colorado Plateau, *Geophys. Res. Lett.*, *35*, L10303, doi:10.1029/2008GL033391.
- Sleep, N. H. (1990), Montegierian hotspot track: A long-lived mantle plume, *J. Geophys. Res.*, *95*, 21,983–21,990.
- Smith, R. L., and R. G. Luedke (1984), Potentially active volcanic lineaments and loci in western conterminous United States, in *Explosive Volcanism: Inception, Evolution, and Hazards*, pp. 47–66, Natl. Acad. Press, Washington, D. C.
- Steinberger, B. (2000), Plumes in a convecting mantle: Models and observations for individual hotspots, *J. Geophys. Res.*, *105*, 11,127–11,152.
- Steinberger, B., and M. Antretter (2006), Conduit diameter and buoyant rising speed of mantle plumes: Implications for the motion of hot spots and shape of plume conduits, *Geochem. Geophys. Geosyst.*, *7*, Q11018, doi:10.1029/2006GC001409.
- Steinberger, B., and R. J. O'Connell (1998), Advection of plumes in mantle flow: Implications for hotspot motion, mantle viscosity and plume distribution, *Geophys. J. Int.*, *132*, 412–434.
- Tagawa, M. (2007), Numerical modeling of slab dynamics: history-dependent rheology and slab stagnation mechanisms, Ph.D. thesis, 218 pp., Hiroshima Univ., Hiroshima, Japan.
- Tian, Y., S.-H. Hung, G. Nolet, R. Montelli, and F. A. Dahlen (2007a), Dynamic ray tracing and traveltime corrections for global seismic tomography, *J. Comput. Phys.*, *226*, 672–687.
- Tian, Y., R. Montelli, G. Nolet, and F. A. Dahlen (2007b), Computing traveltime and amplitude sensitivity kernels in finite-frequency tomography, *J. Comput. Phys.*, *226*, 2271–2288.
- Tian, Y., K. Sigloch, and G. Nolet (2009), Multiple-frequency  $SH$  wave tomography of the western U.S. upper mantle, *Geophys. J. Int.*, *178*, 1384–1402.
- van der Lee, S., and G. Nolet (1997a), Seismic image of the subducted trailing fragments of the Farallon plate, *Nature*, *386*, 266–269.
- van der Lee, S., and G. Nolet (1997b), Upper mantle  $S$  velocity structure of North America, *J. Geophys. Res.*, *102*, 22,815–22,838.
- van der Lee, S., K. Regenauer-Lieb, and D. A. Yuen (2008), The role of water in connecting past and future episodes of subduction, *Earth Planet. Sci. Lett.*, *273*, 15–27.
- Van Wijk, J. W., W. S. Baldrige, J. van Hunen, S. Goes, R. Aster, D. D. Coblenta, S. P. Grand, and J. Ni (2010), Small-scale convection at the edge of the Colorado Plateau: Implications for topography, magmatism, and evolution of Proterozoic lithosphere, *Geology*, *38*, 611–614, doi:10.1130/G31031.1.
- Waite, G. P., R. B. Smith, and R. M. Allen (2006),  $V_p$  and  $V_s$  structure of the Yellowstone hot spot from teleseismic tomography: Evidence for an upper mantle plume, *J. Geophys. Res.*, *111*, B04303, doi:10.1029/2005JB003867.
- Wessel, P., and W. H. F. Smith (1998), New, improved version of the Generic Mapping Tools released, *Eos Trans. AGU*, *79*, 579.
- Wilson, D. C., A. Richard, G. Stephen, J. Ni, and W. S. Baldrige (2010), High resolution receiver function imaging reveals Colorado Plateau lithospheric architecture and mantle-supported topography, *Geophys. Res. Lett.*, *37*, L20313, doi:10.1029/2010GL044799.
- Woodward, R. L., and G. Masters (1991), Global upper mantle structure from long-period differential travel times, *J. Geophys. Res.*, *96*, 6351–6377.
- Xue, M., and R. M. Allen (2010), Mantle structure beneath the western United States and its implications for convection processes, *J. Geophys. Res.*, *115*, B07303, doi:10.1029/2008JB006079.
- Yang, Y., and D. W. Forsyth (2008), Attenuation in the upper mantle beneath Southern California: Physical state of the lithosphere and asthenosphere, *J. Geophys. Res.*, *113*, B03308, doi:10.1029/2007JB005118.
- Yuan, H., and K. Dueker (2005), Teleseismic P-wave tomogram of the Yellowstone plume, *Geophys. Res. Lett.*, *32*, L07304, doi:10.1029/2004GL022056.
- Zhou, Y., F. A. Dahlen, and G. Nolet (2004), Three-dimensional sensitivity kernels for surface wave observables, *Geophys. J. Int.*, *158*, 142–168.
- Zhou, Y., G. Nolet, F. A. Dahlen, and G. Laske (2006), Global upper-mantle structure from finite-frequency surface-wave tomography, *J. Geophys. Res.*, *111*, B04304, doi:10.1029/2005JB003677.

G. Laske, Institute of Geophysics and Planetary Physics, IGPP-0225, University of California, San Diego, La Jolla, CA 92093, USA.

G. Nolet, Géosciences Azur, Université de Nice/Antipolis, 250 Rue Albert Einstein, F-06560 Sophia Antipolis, France.

K. Sigloch, Department of Earth and Environmental Sciences Geophysics, Munich University, Theresienstr. 41, D-80333 Munich, Germany.

Y. Tian, Chevron Energy Technology Company, 6001 Bollinger Canyon Rd., Bldg. D, San Ramon, CA 94583, USA.

Y. Zhou, Department of Geosciences, Virginia Polytechnic Institute and State University, 4044 Derring Hall (0420), Blacksburg, VA 24061, USA.